Influence of Turbofan Engine Design Parameters on Aircraft Environmental Impact

by

Kanghyun Lee

B.S., Seoul National University (2021)

Submitted to the Department of Aeronautics and Astronautics
in partial fulfillment of the requirements for the degree of

Master of Science in Aeronautics and Astronautics

at the

MASSACHUSETTS INSTITUTE OF TECHNOLOGY

June 2023

© Kanghyun Lee 2023. All rights reserved.

Authored by: Kanghyun Lee
Department of Aeronautics and Astronautics
May 23, 2023

Certified by: Steven R.H. Barrett
H.N. Slater Professor of Aeronautics and Astronautics
Thesis Supervisor

Certified by: Raymond L. Speth
Principal Research Scientist
Thesis Supervisor

Accepted by: Jonathan P. How
R. C. Maclaurin Professor of Aeronautics and Astronautics
Chair, Graduate Program Committee

Influence of Turbofan Engine Design Parameters on Aircraft Environmental Impact

by

Kanghyun Lee

Submitted to the Department of Aeronautics and Astronautics
on May 23, 2023, in partial fulfillment of the
requirements for the degree of
Master of Science in Aeronautics and Astronautics

Abstract

Despite the emergence of new energy carriers and propulsion systems architectures, turbofan engines power the majority of commercial aircraft. Therefore, aviation's environmental impacts are significantly influenced by the design of these turbofan engines. Hence, we should drive the design of modern turbofan engines, informed with each design parameter's effect on environmental implications, namely the climate and air quality impacts. To understand the connection between the engine design parameters and an aircraft's environmental impact, it is important to have the capability to quantify the environmental impact resulting from a combined "Aircraft-Engine-Operation" scenario. Through modeling and connecting aircraft, engines, flight operations, emissions, and their resulting impacts on climate and air quality, we can link the end-to-end impact propagation chain and evaluate the outcomes of any engine design alteration. We investigate free design variables such as overall pressure ratio (OPR), fan pressure ratio (FPR), and turbine entry temperature (TET), as well as technology level indicators such as component efficiencies, cooling, and material temperature capability. Sensitivities are calculated for three different reference engines, and the differences in trends between the engines are analyzed. Influence of external-to-aviation uncertainties and valuation choices are also illustrated. Comparison between Jet-A and different sustainable aviation fuels (SAFs) are conducted from an environmental and societal point of view. The study also explores how the derived influence coefficients or sensitivities can provide valuable guidance to stakeholders when making decisions regarding technological investments, design space change, or regulatory assessments.

Thesis Supervisor: Steven R.H. Barrett
Title: H.N. Slater Professor of Aeronautics and Astronautics

Thesis Supervisor: Raymond L. Speth
Title: Principal Research Scientist

Acknowledgments

I would like to first thank my advisor, Steven, for his guidance and support over the past two years. I would also like to thank my project supervisors, Ray, Jayant, and Seb who have played an integral role in my growth and development. I would like to also thank Pratt & Whitney for providing funding throughout my research.

I would like to express my gratitude for my labmates at the Laboratory for Aviation and the Environment (LAE) for creating a welcoming and collaborative environment. Finally, I want to thank my parents for their love and encouragement. Ever since I was 6, aviation has been my life, and I wouldn't have been able to get to this point without their unwavering support.

Contents

List of Figures

List of Tables

Nomenclature

$\dot{m}_f$ Fuel Flow

η_p Component Polytropic Efficiency

D_{p} Mass of regulated pollutants emitted during the standard LTO cycle [g]

F_{00} Rated sea-level static thrust [kN]

X_{cool} Relative cooling flow

ADP   Aerodynamic Design Point

AEIC   Aviation Emissions Inventory Code

AGWP   Absolute Global Warming Potential

ATJ   Alcohol-to-Jet

CI   Confidence Interval

CLB   Climb

CO_2 Carbon Dioxide

CRZ   Cruise

DES   Descent

DR   Discount Rate

EI   Emissions Indices

EIS	Entry Into Service
FPR	Fan Pressure Ratio
FT	Fischer-Tropsch
GDP	Gross Domestic Product
HEFA	Hydroprocessed Esters and Fatty Acids
ICAO	International Civil Aviation Organization
LTO	Landing and Take-off Operation
MTOW	Maximum Take-Off Weight
NO_x	Nitrogen Oxides
NPV	Net Present Value
O_3	Ozone
OEW	Operating Empty Weight
OPR	Engine Overall Pressure Ratio
$PM_{2.5}$	Particulate Matter
PPP	Purchasing Power Parity
PtL	Power-to-Liquid
RCP	Representative Concentration Pathway
RF	Radiative Forcing
RQL	Rich-Quench-Lean Combustor
RTK	Revenue Tonne Kilometer
SAF	Sustainable Aviation Fuel

SFC	Specific Fuel Consumption
SPK	Synthetic Paraffinic Kerosene
SSP	Shared Socio-economic Pathways
TCLA	Turbine Cooling and Leakage Air
TET	Turbine Entry Temperature, T_{t4}
TTW	Tank to Wake
VSL	Value of Statistical Life
WTK	Well to Tank
WTW	Well to Wake

Chapter 1

Introduction

Commercial aviation accounts for $\sim$3.5% (80.4 mW/m^2) of effective radiative forcing (ERF) occurring from anthropogenic emissions [68] and $\sim$24,000 annual premature mortalities [79] due to degraded air quality. With an industry-wide focus on reducing the environmental footprint of aviation, relevant stakeholders, including engine and airframe manufacturers, as well as regulators, are actively pursuing sustainability strategies. As aircraft engines are the dominant source of emissions from aviation, it is important to establish a quantifiable link between engine design parameters or technological advancements and the environmental impact of aviation. This will enable relevant stakeholders to make informed design decisions, technological investments, and establish policies and regulations.

First, we conduct a sensitivity analysis on the primary cycle parameters, specifically the fan pressure ratio (FPR) which has a direct impact on propulsive efficiency, as well as overall pressure ratio (OPR) and turbine entry temperature (TET), which are directly related to thermal efficiency. We also investigate the impact of secondary cycle parameters, namely material temperature capability and cooling weight factor (X_{cool}), as well as the effects of component polytropic efficiencies (η_p). We also assess the influence of external factors, such as discount rates, background emissions scenarios (RCP) and societal scenarios (SSP). Finally, we explore the impact of switching to different sustainable aviation fuels (SAFs).

Several studies have explored the impact of turbofan engine design parameters on aircraft performance and emissions, as shown in Table 1.1.

Table 1.1: Other studies investigating engine design's impact on aircraft performance and emissions.

	Guynn et al. [48–50]	Thoma et al. [88]	Antonie and Kroo [6]	Whellens and Singh [97]	Dinc [24]	This research
Reference baseline engine	CFM56-7B	LEAP-1A	280PAX/6000NM (F_{oo}:350kN, BPR:6)	RB211-524G/H (F_{oo}:250kN, BPR:4.5)	JT9D-7J	CFM56-7B, LEAP-1B GE90-115B
Analyzed design variables	FPR, OPR	FPR, OPR	BPR	FPR, OPR, $T_{4.CRZ}$, $T_{4.Take\text{-}Off}$	T_{t4}, Mach number, component η, LP/HPC PR	FPR, OPR, T_{t4}, material temp. capability, X_{cool}, η, engine weight
Emissions analyzed	CO_2, NO_x, noise	Cruise $\dot{m}_f$ (CO_2) LTO NO_x, noise	Block fuel (CO_2), LTO NO_x, noise	Cruise SFC (CO_2, H_2O, NO_x), LTO NO_x, noise	Cruise $\dot{m}_f$ (CO_2, H_2O, NO_x)	CO_2, NO_x, contrails, H_2O, SO_x, BC, CO, HC, OC
Environmental metric	-	-	-	GWP (simplified)	GWP (simplified)	NPV for climate and air quality impacts
Analysis Point	Full-flight	Cruise & LTO	Full-flight & LTO	Cruise Point	Cruise Point	Full-fleet Full-flight

Guynn et al. [48–50] conducted a FPR and OPR tradeoff study for a single aisle aircraft, exploring both geared fan and direct-drive fan configurations, and determined a fuel-optimum FPR and found that the aircraft mass and block NO_x emission to be minimized with high FPR, and noise and LTO NO_x to be minimized with low FPR. Thoma et al. [88] performed a tradeoff study on OPR and FPR using the LEAP-1A engine model, identifying a fuel-optimal FPR and discovering that increasing FPR leads to higher levels of LTO NO_x emissions, while OPR has a minor impact on SFC but a significant impact on LTO NO_x emissions. Antonie and Kroo [6] optimized an aircraft for minimum LTO NO_x, block fuel, and noise, respectively, finding that there is a BPR yielding minimum trip fuel burn, lower OPR and combustor temperature reduce LTO NO_x emissions, and high BPR reduces noise. Whellens and Singh [97] incorporated CO_2 and NO_x emissions at the cruise point to calculate global warming potential (GWP) and found that a cruise GWP-optimized engine suggests a reduced OPR and T_{t4} compared to the cruise SFC-optimized one. Dinc [24] calculated the percent GWP change from different design parameters using cruise emission on a JT9D-7J engine model.

This research aims to assess the impact of engine design parameters on environmental performance by evaluating the changes in environmental damage attributable to the design alterations. Reporting emission levels alone does not provide a clear understanding of the environmental impact beyond relative change within a given emis-

sion species or compliance with regulations. Therefore, taking the emissions value one step further into quantifying the actual climate and air quality impacts that occur, and thereby understanding the combined environmental damage, provides a more useful understanding of tradeoffs and decision-making.

For stakeholders to compare the economic impacts of different actions or policies and make informed decisions, cost-benefit-analyses (CBA) may be performed. To reflect the true social cost of aviation, we should internalize aviation's externalities. To account for the environmental dimension, environmental costs must be quantified. This is the reason why we intend to quantify the sensitivity of monetized environmental costs (in Net Present Value, NPV) to different engine design parameters. In this study, we consider both climate and air quality impacts as components of the environmental costs. Climate and air quality impacts have different measures, such as RF, GWP, and ΔT_{avg} for climate impacts, whereas air quality impacts are assessed based on factors like increased ground-level pollutant concentrations or premature mortality risk. By having these impacts quantified in common unit of monetary costs, we are able to combine the climate and air quality impacts into a measure of total environmental impacts. Also, setting time preference using a social discount rate (i.e., implicit time horizon) enables us to capture environmental impacts occurring over different timeframes. Additionally, monetizing environmental impacts allows us to compare them with other cost-benefit analysis terms, such as direct operating costs (DOC), noise impacts, and technology development costs, thereby enabling more holistic decision-making.

To reflect the tradeoffs involved, representative schedules are used to perform full-fleet/full-flight calculations of fuel burn and emissions for a given engine-aircraft-operation scenario. For these scenarios, we evaluate a range of engine design parameters and technology level indicators and compute the environmental metric sensitivities. These results are then compared with single-point evaluations. The study also examines how external factors, such as valuation choices or background scenarios, influence the results and ultimately, decision-making. Finally, we compare the social costs of sustainable aviation fuels (SAFs) to those of fossil Jet-A.

Chapter 2

Methods

We introduce the "Engine Environmental Impact" (EEI) framework, which establishes a link between engine design parameters and the resulting aviation environmental impacts. We use this framework to calculate the environmental performance metrics' sensitivity to engine design parameters for different baseline engines. This evaluation involves the following steps: (1) running the aircraft and engine models, including emissions estimation; (2) simulating flights using the engine-aircraft pair of interest and real-world schedules to generate gridded full-fleet/full-flight emissions; (3) applying environmental models to calculate the climate and air quality impact based on the calculated emissions. Through this process, we obtain the quantified results of environmental impact attributable to a given annual emissions scenario, considering a specific engine-aircraft combination and flight operational scenario.

2.1   Aircraft and Engine Model

We calculate the sensitivity of environmental performance to engine design parameters for the three different engines, "A", "B", and "C", which correspond to the CFM56-7B, LEAP-1B, and GE90-115B, respectively. For this study, a Boeing 737-800 aircraft model for engines "A" and "B", and a Boeing 777-300ER aircraft model for engine "C" are developed and used. Engine "A"-Boeing 737-800 represents the current generation narrow-body fleet, engine "B"-Boeing 737-800 represents the next generation narrow-body fleet, engine "C"-Boeing 777-300ER represents current generation wide-body

fleet. These engine-aircraft categories together account for the majority of current aviation emissions. It is important to note that the calculated sensitivity to design parameters will depend on the baseline engine, although similar trends are observable.

In order for the aircraft and engine models to accurately output the necessary performance parameters, they require inputs including the altitude, airspeed, and aircraft's relative mass at each point along a flight profile. At each point across different operating conditions (LTO, climb, cruise, and descent), the aircraft and engine models together output fuel flow, thrust requirement, and rate of climb/descent. The following sections outline the aircraft and engine model used in the study, and how engine design parameters are varied to evaluate the sensitivity of environmental impact to each parameter.

2.1.1 Aircraft Model

To incorporate appropriate engine operation and calculate fuel consumption and emissions, several factors such as aircraft weight, thrust requirements, and airflow must be considered. Therefore, it is necessary to have a corresponding model of the engine-installed aircraft that meets the specified payload and range requirements. Additionally, as engines and aircraft form an integrated system, any changes made to one component can have significant impacts on the other. Any design changes to the engine could result in aircraft-level implications, such as changes in mass or drag, which must be reflected in the tradeoff analysis.

For our aircraft modeling, we utilize the Transport Aircraft System OPTimization (TASOPT) [28], with the engine model replaced with Numerical Propulsion System Simulation (NPSS) [65]. TASOPT, based on first-principle methods, performs conceptual-level design and multidisciplinary design optimization. The aircraft is sized according to the design mission and simultaneously optimized using the Payload Fuel Efficiency Index (PFEI, energy consumption per payload-range), averaged across multiple realistic off-design missions. Initial parameters, including geometry, weight, propulsor, and mission requirements, are provided, and we optimize for the design variables as described by Drela [27]. Design constraints such as minimum

rate-of-climb at top-of-climb, maximum blade temperature, wingspan, and fueltank volume are imposed as penalty functions for the optimizer.

We specify the baseline aircraft, using an iterative process that involves matching the model with real-world aircraft parameters. To ensure that the resulting model is a close approximation of the reference aircraft, penalty functions are utilized to constrain the deviation between the model and actual aircraft data to be within acceptable limits. This accounts for the fact that actual aircraft sizing could have been affected by other considerations, such as the varying requirements for families of aircraft. Closely matching the actual aircraft values also gives confidence in the validity of results. Publicly available data sources, including ICAO EDB [34], 737.org [7], Jenkinson et al. [64], and expert feedback, are used to obtain aircraft and engine data. Modeled aircraft are checked with the real-world data, including OEW, MTOW, weight fractions, fuel tank capacity, payload-range performance, aircraft size and geometry, and engine parameters.

Aircraft performance is calibrated using the payload-range data from Boeing's Airplane Characteristics for Airport Planning [12, 13], specifically using two points as shown in Figure 2-1: one with max payload with shorter range (point A) and the other with max range with maximum fuel capacity (point B).
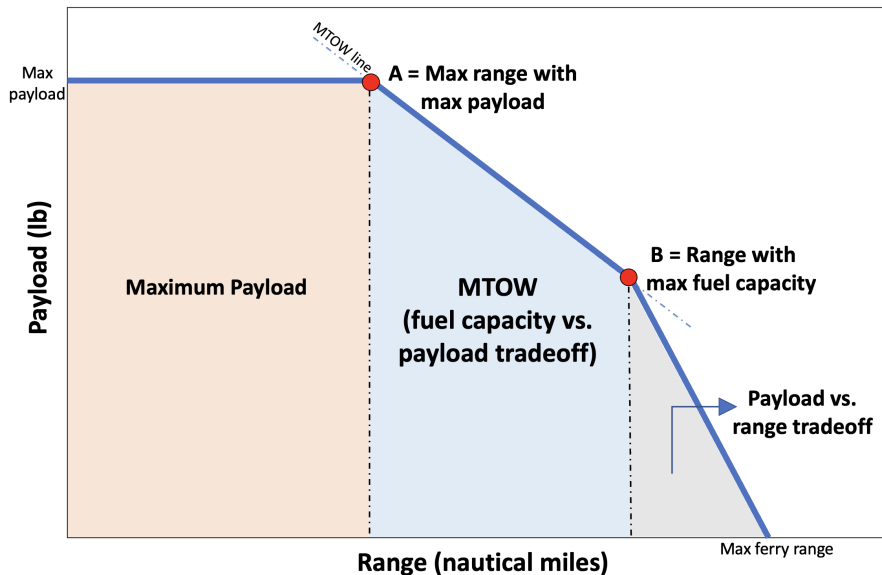
Figure 2-1: Aircraft payload-range diagram.

For engine "A", the B737-800 model is calibrated to a mission range of 2940NM for the maximum fuel capacity MTOW case. For engine "B", the resolved B737-800 airframe from engine "A" is used, and we do not model the improvements in aerodynamics (i.e., advanced winglets) or extra weight caused by the heavier engine (i.e., weight increase in engine struts, wings, fuselage and landing gear). With a lower fuel burn and a fixed fuel tank capacity, engine "B" installed 737-800 results in an extended range capability of 3380NM for the maximum fuel capacity MTOW case. For the B777-300ER aircraft model with engine "C", the maximum fuel capacity MTOW mission range is 7800NM.

2.1.2 Engine Model

In order to accurately simulate and analyze engine performance, it is essential to have an engine model that captures cycle parameters representative of the baseline engines. For all three turbofan engine models developed, a two-spool, separate flow architecture is assumed. Integrating the NPSS engine model with TASOPT essentially allows a Multiple Design Point (MDP) approach spanning key operation points, such as takeoff (SLS), rotation (end-of-runway), climb, cruise, and descent. ADP design point calculation provides component map scaling and nozzle area calculation, followed by off-design performance analyses. The ADP thrust requirement is defined to be between top of climb and cruise thrust requirement, which is optimized for minimum mission fuel burn (i.e., PFEI). A basic schematic of the NPSS architecture used to model the engines are shown in Figure 2-2. The flow is modeled to be split into core and bypass before the fan, with fan root compression attributed as part of LPC.
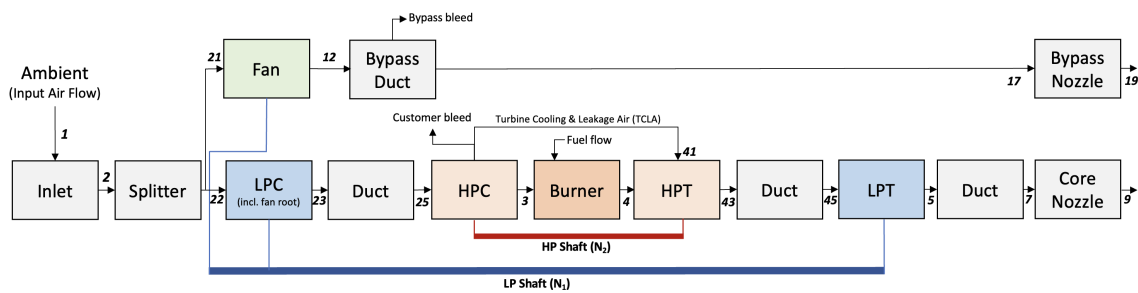
Figure 2-2: NPSS engine model schematics, including station numbering.

To converge to a solution using NPSS [65], $\dot{m}_f$, $\dot{m}_\text{air}$, and BPR are varied to meet prescribed thrust, T_t4/T_t2, and fan diameter targets. As a result, BPR is considered to be an output parameter of the engine sizing process. Also, turbine cooling and leakage air (TCLA) is varied to meet a specified end-of-runway metal temperature limit. Component polytropic efficiencies and combustor fractional pressure loss are estimated using expert and industry feedback. The resulting engine is checked to be within 2.5% relative RMS error from the ICAO EDB [34] in terms of $\dot{m}_f$-F_N SLS (uninstalled) data points. Final engine models are also compared with other studies when available, specifically focusing on engine parameters such as FPR, LP/HPC PR, η_p, thrusts, and SFC. Compared literature include York et al. [103], in which the original TASOPT engine models were used to model the CFM56-7B and GE90-94B. FPR and HPC pressure ratio values for CFM56-7B and LEAP engines are referenced from Georgia Tech's NPSS models [73].

FPR and component efficiencies for the LEAP-1B/B737-8MAX are compared with Thacker and Blaesser [87]. HPC pressure ratio for LEAP-1B and GE90-115B are referenced from Wadia [95]. GE90-94B's FPR, OPR (and LP/HPC PR), T_4, LPT η_p values from Dewanji et al. [23] and Díez et al. [30] are used to infer the parameters of the GE90-115B engine model. SFC of CFM56-7B and GE90 engines, and GE90's HPC pressure ratio are compared with data from Jane's Aero Engines [63]. Cycle temperatures (i.e., T_t4) and non-chargeable cooling flow (TCLA_NC) fraction are set referring to FAA Type Certificate Data Sheets (TCDS) [38–40], where the maximum limits for the turbine exit temperature (T_{49}) or the LPT inlet temperature (T_{45}), and the maximum permissible bleed air extraction are provided.

Bare engine weight is estimated using Torenbeek's model [89], which takes in net thrust (F_N), total airflow in ($\dot{m}_\text{air}$, in lbm/sec), BPR, and OPR as inputs as follows:

$$W_\text{Eng.Bare} \text{ (lb)} = \frac{10 \cdot \dot{m}_{air}(\text{OPR})^{0.25}}{1 + \text{BPR}} + 0.12 \cdot F_\text{N}\left(1 - \frac{1}{\sqrt{1 + 0.75 \cdot \text{BPR}}}\right)$$

Engine weight is calibrated at design mission's SLS takeoff condition. For nacelle and nozzle weight, the TASOPT weight model [77] is used, which takes in OPR,

BPR, and core mass flow ($\dot{m}_{\text{core}}$). Based on fraction of bare engine weight, additional equipment weight (10%) and pylon weight (5%) are added.

Bleed air, namely turbine cooling & leakage air (TCLA) with a cooling model, and customer bleed are modeled. Although bypass leakage flow is modeled, all turbine cooling bleeds are assumed to be extracted from the HPC (neglecting bypass bleed) with bleed tap information obtained from public data sources [17, 31–33, 41]. Bleed flow is modeled by specifying a fractional bleed pressure depending on the stage where bleed flow is extracted from. TCLA flow is divided into non-chargable (model connection to HPT inlet), and chargeable (model connection to HPT exit) parts. The cooling model is implemented from the semi-empirical NASA CoolIt algorithm [43], where cooling flow is estimated as:

$$W_{\text{cool}} = X_{\text{cool}} \cdot W_{\text{hot}} \left(\frac{\phi_{\text{adjusted}}}{1 - \phi_{\text{adjusted}}} \right)^{1.25}$$

Here, W_{cool} is the bleed flow needed to satisfy a prescribed cooled temperature target, W_{hot} is hot gas mass flow rate, ϕ_{adjusted} is the cooling effectiveness (ϕ) corrected for pattern factor, and X_{cool} is the relative cooling flow. Note that when modeling the baseline engines, we input a cooled HPT η_{p} that already includes the expected efficiency drop. HPT blade/vane metal temperature at ADP is set to meet the maximum metal temperature limit which occurs at end-of-runway takeoff condition. Customer bleed and generators are modeled using a fractional value of payload and MTOW. Although we expect the customer bleed requirement to be smaller at low altitudes (due to less cabin pressurization requirement), and TCLA requirement to be lower at cruise compared to takeoff, customer bleed flow (lbm/s) and TCLA (% of primary airflow) are kept constant throughout all operating conditions, due to a lack of detailed data.

2.1.3 Varying Engine Design Parameters

We explore a range of engine design parameters that we anticipate will have a significant impact on the environmental performance of aircraft engines. By examining the

sensitivity of environmental performance metrics to these parameters, we can gain a better understanding of the tradeoffs that each respective parameter causes.

In our investigation, we identify OPR, FPR, and TET as primary cycle design parameters of-interest, as they play a significant role in determining the overall efficiency of the engine. Higher OPR and TET generally result in greater thermal efficiency, while a lower FPR leads to higher propulsive efficiency. However, higher OPR can also lead to increased NO_x emissions, resulting in a CO_2-NO_x tradeoff, and lower FPR can have implications for engine weight, drag, and installation. Additionally, higher TET is associated with an increase in cooling flow and associated loss in HPT cooled efficiency.

We also focus on secondary cycle parameters, such as material temperature capability and relative cooling flow (X_{cool}), which can impact the engine components' ability to withstand high temperatures and stresses. These factors can have significant effects on the engine's lifespan, overall efficiency, and emissions. Finally, we investigate the sensitivities of the engine's component polytropic efficiencies (η_p) and weight, as they are directly related to reducing fuel consumption and emissions.

Individual design parameters are varied while the rest are kept fixed. Throughout all engine tradeoff explorations, we assume a fixed aerodynamic design point (ADP), which includes a specified altitude, Mach number, and thrust level. Thrust requirements at all off-design operating points are also assumed to be fixed throughout the analysis. However, for the FPR, OPR, and engine weight tradeoffs, change in engine weight or nacelle drag (for FPR variation) require aircraft weights and thrust requirements to be recalculated (fixed flight path angle is assumed). The engine design parameters investigated can be divided into two categories: free design variables (OPR, FPR, and TET), and technology levels (material temperature capability, cooling technology, and turbomachinery component efficiencies). T_{t4} (except for TET tradeoff), and fan diameter (except FPR tradeoff), are fixed at ADP. Material temperature capability (using HPT blade metal temperature at rotation/end-of-runway as a surrogate), is kept constant, except when analyzing its impact.

For FPR variations, BPR and fan diameter are varied to reach a fixed jet velocity ratio $\left(i.e., \frac{V_{\text{Nozzle.Bypass}}}{V_{\text{Nozzle.Core}}}\right)$ at ADP. Thrust requirements are recalculated iteratively using TASOPT to incorporate changes in weight and drag of the engine and the aircraft. Geared fans or variable area nozzle (VAN) technology, which can be employed in low FPR designs, are not explored in this study.

For OPR changes, the pressure ratio split between the LPC and HPC is kept constant, as we do not observe a noticeable change by varying LPC/HPC work split, other than results reflecting LPC/HPC η_p difference. For TET, material temperature capability, and X_{cool} tradeoffs, we account for the change in HPT cooled efficiency $(\Delta\eta)$ from a change in cooling flow. Based on calculations performed by Horlock and Torbidoni [54], using the analytical model developed by Hartsel [51], an increase of 1% in cooling flow (relative to the primary flow) is assumed to cause a reduction of 0.36 percentage points in the HPT cooled efficiency (η_p). For OPR tradeoff, we do not consider the HPT η_p loss although the cooling flow fractions are also affected by variations in OPR, as its impact is relatively less compared to other dominant factors of OPR tradeoff. For TET tradeoffs, it is also important to note that changes in TET are modeled to have no effect on NO_x emission as a P3T3 method with no FAR exponent is used (which may not be true for engines with high T_{t4}, where NO_x generation can no longer be seen as being solely a function of combustor inlet temperature).

For cooling technology tradeoffs, relative cooling flow (X_{cool}) is varied. Except in cases where a specific component polytropic efficiency (η_p) is changed to evaluate its impact, component polytropic efficiencies are held constant as they are considered to be technology level indicators.

2.2   Aviation Emission Inventory Generation (AEIC)

The Aviation Emissions Inventory Code (AEIC) is utilized to generate an inventory of fuel burn and emissions for an annual aircraft-engine-operation scenario. AEIC takes in aircraft performance data, engine emissions data, and flight schedules, and

computes flight profiles and fuel/emissions, as described in Simone et al. [84] and Stettler et al. [85]. The TASOPT-NPSS aircraft-engine model introduced earlier is employed to provide the aircraft performance data. The generated emissions inventory includes NO_x, CO, BC, and OC along with fuel burn and flight distances, with a spatial resolution of $1° \times 1° \times 200$ ft with the vertical resolution decreased to 1000 ft above 1000 ft.

We assume a weight load factor of 70% maximum payload, as per recent IATA data [62], and cruise altitude is assigned using a triangular distribution with a central value of 7000 feet below the service ceiling with maximum altitude constraint from aircraft performance taken into account. Note that step-climb is not modeled. The lateral route is assumed to be a great-circle route between the origin and destination. Flight schedules are obtained from 2019 OAG schedule data [47], with filters applied for the corresponding aircraft category and range. Note that accurately capturing the distribution of real-world flights is especially important for air quality impact calculations.

AEIC simulates flights by dividing a flight profile into two portions: LTO (≤ 3000 ft) and non-LTO (>3000 ft). For LTO operations, calculations are performed using an airport-specific "time-in-mode (TIM)" method, which assumes specific power levels (percentage of F_{00}) for each LTO cycle phase [85]. TIM is estimated using method from Watterson et al. [96], with departure divided into taxi-out, taxi-acceleration during taxi-out, before takeoff hold, takeoff and initial climb, and climb out, and arrival TIM divided into approach, landing, reverse thrust, taxi-in and taxi acceleration during taxi-in. For non-LTO operations, including climb, cruise, and descent, calculations are performed on a flight-path-specific basis using aircraft performance data such as the fuel flow and EI(NO_x), calculated using inputs of true airspeed (TAS), rate of climb/descent for each altitude and aircraft mass level.

2.2.1 Emission Estimation

Engine emissions except for NO_x and nvPM are modeled following Simone et al. [84] and Stettler et al. [85]. Emissions are modeled using methods that estimate at-altitude

emissions referring to ICAO EDB ground emissions measurement data [34].

When we change the engine design parameters from the baseline values, fuel flow and $EI(NO_x)$ are recalculated to fully capture the impact of engine design change on CO_2, SO_x, H_2O and NO_x emissions. However, we assume that the EIs of other species (CO, HC, and PM) are assumed fixed, meaning that we partially capture the effects on these emissions species through change in fuelflow. For scenarios where sustainable aviation fuels are used, emissions are adjusted per Table 2.3.

CO_2, SO_x, H_2O

Carbon dioxide (CO_2), sulfur oxide (SO_x), and water vapor (H_2O) emissions are directly calculated from fuel flow. For conventional Jet-A fuel, $EI(CO_2)$ of 3.155 kg/kg (complete combustion assumed) is applied, consistent with FAA's ACCRI Phase II report [14]. Lifecycle CO_2 emissions (well-to-wake, WTW), including direct combustion or tank-to-wake (TTW) emissions and well-to-tank (WTT) are considered depending on fuel types, as discussed in Section 2.5. For SO_x emissions, we assume a fuel sulfur content of 600 ppm by mass with a 2% sulfate conversion efficiency [85]. $EI(H_2O)$ of 1.233 kg/kg is applied, as per FAA's ACCRI Phase II report [14].

NO_x

NO_x emissions do not scale linearly with fuel flow and cannot be assumed with a constant emission index (EI). NO_x LTO emission measurement data from ICAO EDB [34] can be used to estimate at-altitude NO_x emissions. We use a semi-empirical P3T3 method from Dubois and Paynter [29]:

$$EI(NO_x)_{Alt} = EI(NO_x)_{SL} \left(\frac{P_{3,Alt}}{P_{3,SL}}\right)^n \left(\frac{FAR_{Alt}}{FAR_{SL}}\right)^m \exp\left[19(h_{SL} - h_{Alt})\right]$$

$n = 0.4$ is used as suggested by the empirical data [29]. $m = 0$ is used, the value suggested for a conventional rich front end single annular combustor [29]. We note that the value for m for engine "B" is requires further investigation, as it is equipped with lean-burn combustor. h_{SL} and h_{Alt} are the humidity ratio of air at sea-level

and at-altitude conditions, respectively ($kg_{H_2O}/kg_{dry\ air}$). The humidity correction is applied to account for increased water content in combustor inflow reducing the peak flame temperature (i.e., less NO_x) [29]. We assume a relative humidity of $\phi = 60\%$ for at-altitude ambient conditions. The value 19 inside the exponential humidity correction term was originally proposed based on experimental data obtained using Pratt & Whitney JT9D engine's advanced annular combustor [71, 82]. This value falls within the range of 12.01 to 24.35 (mean: 18.68), which was obtained using 30 different types of engines [25].

With the NPSS engine models informing combustor inlet condition (T_3, P_3), the reference engine's $EI(NO_x)$ data from the ICAO EDB [34] is used to generate a polynomial curve fit. Throughout design tradeoff calculations for a given engine, we use the same P3T3 NO_x correlation assuming that the combustor design remains fixed and a change in combustor inlet condition occurs [29].

Figure 2-3 shows the NO_x emission measurement data from ICAO EDB [34] for the three reference engines and the P3T3 curve fit. We show the combustor operating points for reference cruise (FL350, for high/ref/low mass levels), and climb (FL100-FL350) cases. The P3T3 correlation emanations are presented in Appendix A.
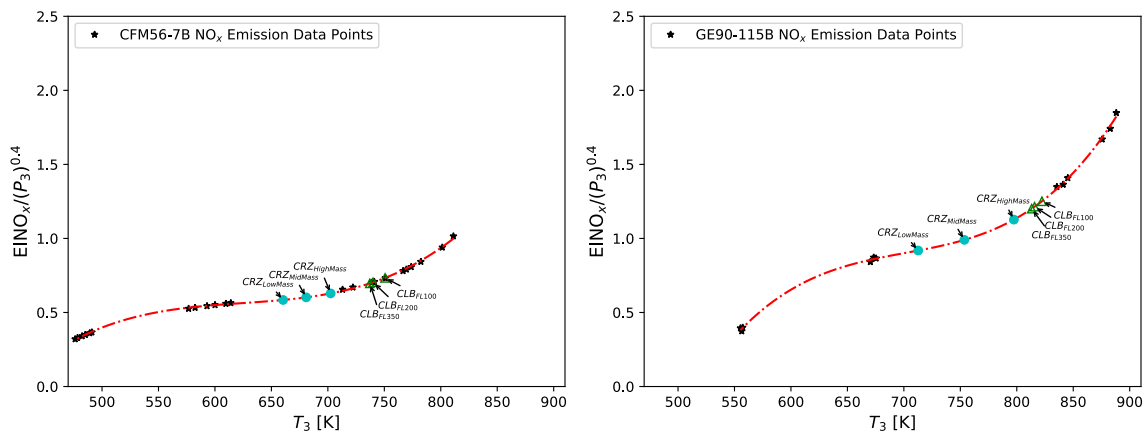
Figure 2-3: P3T3 NO_x model for engine "A" (left), and engine "C" (right).

Engine "B", which references the LEAP-1B engine, poses a challenge in $EI(NO_x)$ estimation due to the lean burn-staged TAPS II combustor's two distinct operating modes combined with the significant gap in emission measurement data between 30%

31

and 85% F_{00}. Hence, it is inadequate to simply fit all data points to a single curve for engine "B". To address this issue, three possible NO_x emission curves are developed to reflect the high uncertainty regions, as shown in Figure 2-4.
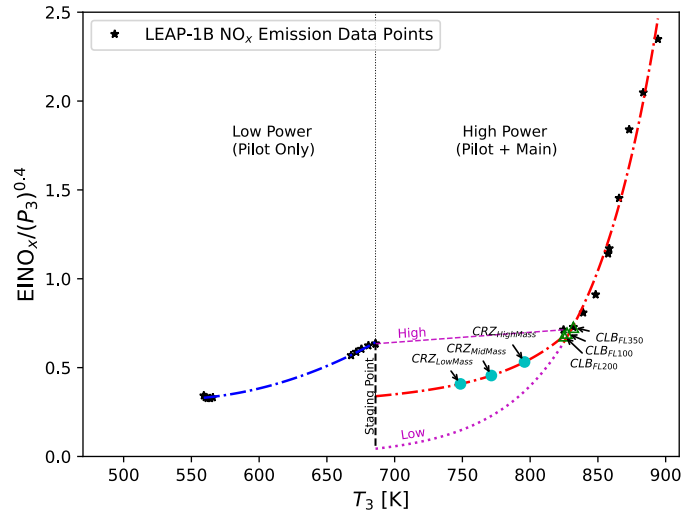
Figure 2-4: P3T3 NO_x model for engine "B". Due to high uncertainty between the last 30% F_{00} and the first 85% F_{00} data point, lower and upper bounds are shown for this region.

We assume that the staging occurs at the N1 spool speed of the highest 30% F_{00} ($N1_{stage} = 60\%$) but aim to bracket the uncertainty in this region by having a low NO_x bound from an exponential fit through the high-thrust points, a high NO_x bound connecting the two data points as a straight line, and a mid-NO_x case using the mean value between the low and high bounds. A polynomial fit is used for the low power mode, and an exponential fit is used for the high power mode where data points exist. We should stress the need for more availability of lean burn-staged combustor NO_x data to reduce this uncertainty, particularly as most cruise operating points fall within this uncertain region (Figure 2-4).

Other Emissions (CO, HC, OC, nvPM, Contrails)

EI(CO) and EI(HC) are computed using the Boeing Fuel Flow Method 2 (BFFM2) [10, 85] method with log-fitting corrections [66].

The non-volatile PM (nvPM) method is updated to use the "Mission Emissions

Estimation Methodology" (MEEM) [3]. Emission index for organic carbon (OC), a subcategory of volatile PM emissions, is divided into two categories. EI(OC) due to incomplete combustion, or EI(OCIC), is estimated as mean 20 mg/kg$_{\text{fuel}}$, and EI(OCLO) from lubrication oil is added so that EI(OCLO) account for 15% of total EI(OC) at low thrust settings and 50% of total EI(OC) at high thrust settings [85]. Contrail impacts are modeled to scale with flight distance, with no sensitivity to engine or aircraft parameters, as flight-by-flight contrail impact attribution is still an active area of research.

2.3   Climate Impact Modeling

Aviation climate impacts depends on the quantity of each emission species emitted, atmospheric residence time, radiative forcing, and temperature response. This is quantified using the Aviation Environmental Portfolio Management Tool - Impacts Climate (APMT-IC) v24c [46, 69, 70, 101, 102].

APMT-IC first computes the global radiative forcing (RF) attributable to a given annual aviation emissions scenario. Temperature model then links this RF to global average temperature change, or ΔT_{avg}. The resulting percentage GDP change due to predicted ΔT_{avg} is estimated using climate damage functions. Finally, the calculated GDP percentage change is multiplied with GDP forecasts from shared socio-economic pathways (SSPs) [22] to obtain climate impact results.

Modeling details are described in Grobler et al. [46], however we do incorporate recent updates on NO_x-induced aerosol impacts, contrail impacts, NO_x-CH_4 pathway, and climate damage functions. First, the NO_x-induced aerosol RF is updated to a mean value of -3.1 mW/m^2 (per Tg N) from Prashanth et al. [78], with a uniform uncertainty distribution of $[-4.4, -1.8]$ mW/m^2 to keep the relative uncertainty range consistent as before. We use the terms "NO_x-induced aerosol" instead of "Nitrate aerosol", as it was found that NO_x emissions are responsible for multiple aerosol species including but not limited to Nitrate aerosol [78]. Secondly, contrail-cirrus radiative efficacy (ERF/RF) is updated to a triangular distribution with a central

value 0.417 [0.31-0.59], consistent with Lee et al. [68]. Contrail-cirrus RF values are updated to a triangular distribution of central value 69.78 [20.9-118.62] mW/m^2 for the reference emission year 2006 [11, 15, 18, 83]. We apply a scaling factor of 1.23 to AGWP$_{100}$ value of NO$_x$−CH$_4$ pathway to account for shortwave CH$_4$ forcing effects [36, 68]. Lastly, we use an updated climate damage function from Howard and Sterner [55] aligned with recent global social cost of carbon estimates in literature consistent with Hänsel et al. [56]. As pointed out in Dray et al. [26], while the updated damage function results in a social cost of carbon that is about 2.8 times higher than the previous APMT-IC (using the DICE 2017 damage function [76]), the revised social cost of carbon is consistent with current global estimates of the social cost of carbon found in literature.

APMT-IC has the capability to include lifecycle emissions, namely CO$_2$, N$_2$O, CH$_4$. However, the results presented in this paper take inputs of the CO$_2$e lifecycle emissions values from LCA analyses, which implicitly includes all well-to-tank (WTT) emissions. For Jet-A, well-to-tank (WTT) CO$_2$ emissions are accounted for by subtracting direct combustion (tank-to-wake, TTW) CO$_2$ emissions from the total lifecycle emissions (well-to-wake, WTW) of Jet-A (89 gCO$_2$e/MJ [61]). For SAF, direct combustion (tank-to-wake, TTW) CO$_2$ is set to zero, with their total lifecycle CO$_2$ emissions values (Table 2.1) considered as well-to-tank (WTT) emissions. Climate impact of well-to-tank (WTT) CO$_2$ emissions are incorporated as direct radiative forcing, and calculated with the RF transfer functions from Etminan et al. [36].

Impacts are estimated on a year-by-year basis, which is then discounted using the net present value (NPV) approach. Note that all results within this paper, unless mentioned otherwise, are based on the RCP4.5 and SSP2 scenario (i.e., SSP2-4.5) with a 3% discount rate. A quasi-Monte Carlo approach is used to generate results using a Sobol set of 10,000 members, where convergence in terms of relative standard error of sample mean was found to be within 2.5% for both climate and air quality impact results [46].

2.4 Air Quality Impact Modeling

Ozone (O_3) and particulate matter ($PM_{2.5}$) at ground-level are pollutant species of concern, that are known to have human health impacts [46]. Air quality impacts are modeled following the approach of Grobler et al. [46], with updates on ozone concentration response function (CRF), baseline incidence rates, population data, and global-average VSL.

The emission-to-exposure marginal sensitivity on a global domain is computed using the adjoint of a chemistry-transport model (CTM), namely the GEOS-Chem adjoint v35 [52]. These sensitivities are computed on a global grid, representing the change in annual average population weighted concentration due to a change in each specific emissions species, with units of $\left[\frac{(\text{ppbv of } O_3) \text{ or } (\mu g \text{ of } PM_{2.5})}{\text{kg/hr}} \right]$.

2.4.1 Computing Change in Concentration

The GEOS-Chem adjoint is assigned an output of interest as an objective function (population-weighted ground-level concentrations of O_3 and $PM_{2.5}$), which it computes from the forward model outputs, and then calculates the sensitivity (first derivative) of this objective function to input emissions according to chemical species, location, and time. GEOS-Chem adjoint simulations are performed on a 4° (latitude) × 5° (longitude) grid, with 47 vertical hybrid sigma-eta pressure levels from the surface up to 0.01 hPa ($\sim$80 km).

For aviation emissions, the FAA AEDT 2015 dataset [67, 100] was used. For global non-aviation anthropogenic emissions, we used the EDGAR 2010 4.3.1 [19], and substitute it with regional emission inventories such as the U.S. EPA NEI 2011 [93] where available. Lightning NO_x emissions were calculated using observation-corrected convective cloud depth [75], while wildfire emissions were taken from the GFED4 inventory [80]. Dust Entrainment and Deposition (DEAD) mobilization scheme by Zender [104] and sea-salt simulation model by Alexander [4] were used. HC emissions from aircraft engines were speciated into the constituent hydrocarbons in alignment with EPA [92].

Figure 2-11 presents the GEOS-Chem Adjoint result: the sensitivity of annual average, population weighted O_3 and $PM_{2.5}$ concentration increase due to aviation NO_x emissions. Note that these sensitivities do not indicate where air quality impacts are occurring, but rather give the contribution to global air quality impacts attributed to emissions at those locations. Although we only visualize the sensitivity to NO_x as it accounts for more than 90% of total air quality impacts, other emission species that contribute to increase in O_3 and $PM_{2.5}$ concentration, namely NO_x, SO_x, BC, HC, CO, and OC, are also included.
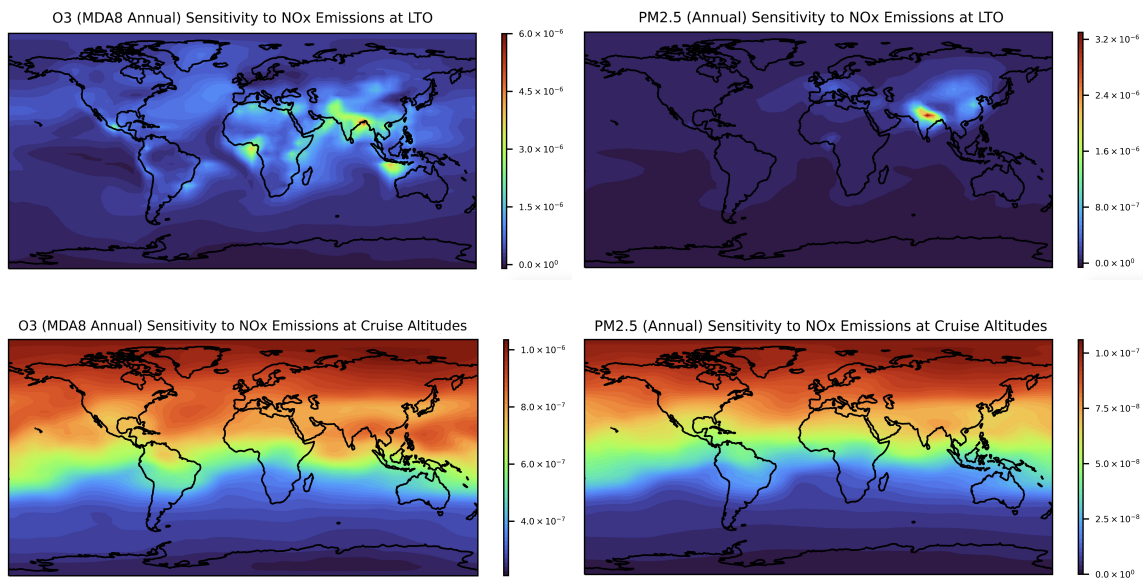
Figure 2-5: Sensitivity results from NO_x emission to increase in "annual average, population weighted concentration" of O_3 MDA8 and $PM_{2.5}$, for LTO (averaged over 0-1 km in altitude) and cruise (averaged over 9.4-12.6 km in altitude), computed using the GEOS-Chem Adjoint.

For this study, the adjoint sensitivity matrix of each emission species is multiplied with the aviation emissions dataset produced using AEIC to calculate the increase in ground-level O_3 and $PM_{2.5}$ exposure.

2.4.2 Mortality Derivation and Valuation

To calculate the premature mortalities related to O_3 and $PM_{2.5}$, we use a log-linear concentration response functions (CRF) from epidemiological literature. For ozone,

CRF from a long-term ozone exposure study is used, where it found a 10 ppbv increase in annual-average O_3 (MDA8) resulted in a 12% increase (95% CI: 8.0-16%) in respiratory mortality rates [90]. For $PM_{2.5}$, we use CRF from a meta-analysis of epidemiological studies that found a 10 µg/m^3 increase in annual-average $PM_{2.5}$ to be associated with an 11% increase (95% CI: 5.0-16%) in cardiovascular mortality rates [53]. Global population (age 30+) is obtained from 2019 Global Health Data Exchange data [42], which is replaced with population data from shared socioeconomic pathways (SSP) scenarios [22] for future years. Note that population projection uncertainty is not separately accounted for. Baseline mortality rates for age group 25+ are also taken from 2019 Global Health Data Exchange data, with chronic respiratory disease mortality rate ($= \frac{\text{deaths}}{100,000 \text{ population}}$) of 86.56 (lower: 77.99, upper: 93.72) and respiratory disease mortality rate of 404.56 (lower: 372.20, upper 429.87) [42].

To monetize the societal impacts of aviation-related premature mortalities due to air pollution, we use the value of statistical life (VSL) approach as per Barrett et al. [9] and Grobler et al. [46]. Global-average VSL approach is used as the difference in results compared to a country-specific VSL approach was reported to be less than 3% [46]. Global-average VSL is calculated for a given valuation year (value yr) and a set dollar year ($ yr), based on the US EPA's meta-study estimate (1990 US VSL of 4.8 million USD_{1990} [1]). This VSL is inflation-adjusted by using a GDP deflator for the U.S. from Federal Reserve data [91] and fitting a Weibull distribution to it with a scaling of 7.75 and a shape factor of 1.51, per EPA guidelines [94]. Also, we adjust for Real Gross Domestic Product (GDP) per capita for the U.S. from Federal Reserve data [91], using an income elasticity (ε) of 0.7 [2, 81]. Hence, to calculate US VSL in a particular valuation year and dollar year, we use the formula:

$$\text{VSL}_{\text{US,value yr,\$ yr}} = \text{VSL}_{\text{US,1990,1990}} \times \left(\frac{\text{GDP}_{\text{deflator,value yr}}}{\text{GDP}_{\text{deflator,1990}}} \right) \times \left(\frac{\text{Real GDP}_{\text{pc,\$ yr}}}{\text{Real GDP}_{\text{pc,1990}}} \right)^{\varepsilon}$$

From this US VSL, we then derive a country-specific VSL as:

$$\text{VSL}_{\text{country}} = \text{VSL}_{\text{US,value yr,\$ yr}} \times \text{IR}_{\text{country}}^{\varepsilon}$$

$$\text{IR}_{\text{country}} = \left(\frac{\text{GDP}_{\text{PPP, country}}}{\text{GDP}_{\text{PPP, US}}} \right)$$

where the income ratio (IR) is obtained by normalizing the GDP (PPP) per capita with the US GDP (PPP) per capita. The GDP (PPP) per capita data for all countries are taken from World Bank [8].

This results in a global-average VSL ($= \frac{\sum(\text{VSL} \times \text{Population})_{\text{country}}}{\sum(\text{Population})_{\text{country}}}$) of 6.99 (95% CI: 1.12-15.97) million 2019 USD. Cessation lag is applied in accordance with US EPA recommendation [35], with 30% of mortality occurring the first year after emission, 50% uniformly distributed $2 - 5$ years after emission, and 20% occurring between $6 - 20$ years after emission. Monetized costs for premature mortality are discounted using discount rates of choice, and a coupled Monte-Carlo simulation with 10,000 members is employed to align with the climate model.

2.5   Sustainable Aviation Fuel (SAF) Modeling

While the environmental cost sensitivity may be sufficient for analyzing the externalities of aviation when assuming the use of fossil jet fuel, a more comprehensive analysis may be necessary when considering alternative jet fuels. For example, when comparing SAFs to fossil jet-A, the fuel production may have different social and economic costs that need to be incorporated for assessments. Hence, we include the marginal cost of fuel production in the quantification of the social costs of aviation, as fuel production consumes resources that can be otherwise reallocated for different purposes.

We conduct a comparison between the fossil jet fuel and different types of SAF. As we do not consider an airframe change in this study, fuel comparisons are limited to drop-in fuels. We account for the fuels' life-cycle emissions from life-cycle analyses (LCA) and production costs. For the SAF cases, we also modify the emissions accordingly. We calculate the climate and air quality costs using the SAF's life-cycle emissions and modified emissions, obtaining the total environmental costs. Then, we add the marginal cost of fuel production to obtain total social costs.

For Jet-A, we use 89 gCO$_2$e/MJ [61] as the life-cycle emissions. Jet-A's marginal

cost of production is estimated from market prices using the Lerner Index, which is a measure of market power, following Miller et al. [74]. Market price of Jet-A is approximated as a uniform distribution of 50 to 150 [USD$_{2019}$/Barrel] for all analyses referencing IATA Jet Fuel Price Monitor [57] from January 2015 to June 2022.

As shown in Table 2.1, nine different types of SAFs, namely vegetable oil & crops hydroprocessed esters and fatty acids (HEFA), waste fats, oils and grease (FOGs) HEFA, municipal solid waste (MSW) Fischer-Tropsch (FT), lignocellulosic FT, crop residues FT, forest residues FT, sugarcane advanced fermentation (AF), residues alcohol-to-jet (ATJ), and power-to-liquid (PTL) are considered.

Table 2.1: SAF lifecycle emissions (LCA) and production costs (from Ref. [5, 26, 37, 59, 60]). If minimum and maximum values are presented inside brackets if available.

Forecast Year	2020	2020	2050	2050
Pathway	LCA (gCO$_2$e/MJ)	Prod. costs (2020 USD/L Jet-A eq.)	LCA (gCO$_2$e/MJ)	Prod. costs (2020 USD/L Jet-A eq.)
Veg. oil crops HEFA	45.1	1.4	29.1	1.3
FOGs HEFA	20.1	0.9	5.8	0.8
MSW FT	27.6	1.1	38.2	0.9
Lignocellulosic FT	27.8	[1.3, 1.5, 1.8]	16.8	[1.1, 1.3, 1.6]
Crop residues FT	12.7	[1.2, 1.4, 1.5]	10.9	[1.0, 1.2, 1.3]
Forest residues FT	7.7	[1.2, 1.3, 1.5]	7.2	[1.0, 1.1, 1.3]
Sugarcane AF	10.7	[1.2, 1.4, 1.7]	3.8	[1.1, 1.3, 1.6]
Residues ATJ	[24.6, 40]	1.11	-	0.72
Power-to-Liquid (PtL)	[15, 18]	[2.69, 3.22]	[12, 18]	[1.09, 1.36]

Biofuel production costs and LCA data are from Dray et al. [26], unless mentioned otherwise below. For PtL, the LCA values are from the 2022 ICAO LTAG report [60] and production costs are from Falter et al. [37]. For ATJ, the LCA values are from 2021 ICAO CORSIA report [59], 2020 production costs are from Geleynse et al. [44], and 2050 production costs are from the ICF report for ATAG Waypoint 2050 [5].

Lifecycle emissions of the respective SAF, including emissions attributable to pro-

cesses such as feedstock production, feedstock-to-fuel conversion, transportation, and land use change are accounted for [26]. Similarly, production cost of SAFs result from a techno-economic analysis modeling each step of the supply chain, including costs for utility, feedstock production, refinery financial assumptions, transportation, and land use change [26]. Future projections of SAF lifecycle emissions and production costs reflect increased use of lower emissions/cost production methods and energy sources.

SAF has different fuel composition and emissions from Jet-A, mainly leading to lower levels of soot and sulfur dioxide emissions. Emissions for SAFs are modified as shown in Table 2.2, as per Stratton et al. [86], where synthetic paraffinic kerosine (SPK) fuel's emissions relative to Jet-A was studied, with the exception of NO_x, where we assume unity.

Table 2.2: Emissions/RF fractional multipliers for 100% SPK fuels [86].

CO_2	0.98
NO_x	1
H_2O	1.1
SO_x	0
Soot	$[0.05 - 0.40]U$
Contrail-cirrus	1

Caiazzo et al. [16] found a paraffinic biofuel's net contrail RF difference from fossil Jet-A to range between -4% and $+18\%$, while Dray et al. [26] used a triangular distribution of 0.58 (lower bound: 0.19, upper bound: 1.18) as a RF multiplier to fossil Jet-A's contrail impact based on a literature survey. However, observational evidence of change in contrail impact from using SAF is not yet established (although it is established that SAF has a higher water vapor EI and results in reduction in soot particle emissions). As SAF's impact on contrails is an area of active research, we take the conservative approach of assuming SAF's contrail impact to be unchanged from that of conventional Jet-A, therefore primarily focusing on the effect of lifecycle CO_2 emissions reduction of SAF. We assume energy density of 43.2 MJ/kg for conventional Jet-A and 44.1 MJ/kg for paraffinic SAFs.

Chapter 3

Baseline Engine Results

3.1 Engine and Aircraft Model and Validation

The results for the developed engine-aircraft models are presented in Table 3.1.

Table 3.1: Resulting baseline engines for design tradeoff studies.

Engine	"A"	"B"	"C"
Reference (EIS)	CFM56-7B (1997)	CFM LEAP-1B (2017)	GE90-115B (2004)
SLS 100% F_{00} [kN]	121 (27290 lbf)	130 (29316 lbf)	514 (115531 lbf)
Fleet simulation Airframe	Boeing 737-800	Boeing 737-800	Boeing 777-300ER
OPR	28.4 (LP: 3.06, HP: 9.29)	44.5 (LP: 2.21, HP: 20.17)	39.9 (LP: 1.86, HP: 21.46)
FPR	1.690 (BPR: 4.9)	1.585 (BPR: 8.5)	1.600 (BPR: 7.2)
T_{t4}/T_{t2}	6.12	6.67	6.20
SFC $\left[\frac{kg}{N \cdot s}\right]$	1.806×10^{-5} (0.638 lbm/hr/lbf)	1.578×10^{-5} (0.568 lbm/hr/lbf)	1.657×10^{-5} (0.585 lbm/hr/lbf)
Alt_{ADP} [m]	10668 (35000 ft)	10058.4 (33000 ft)	9753.6 (32000 ft)
$F_{\text{N.ADP}}$ [kN]	22.4 (5035 lbf)	25.1 (5652 lbf)	98.0 (22019 lbf)
$W_{\text{Eng.Bare}}$ [kg]	2209 (4870 lb)	2255 (4972 lb)	9066 (19987 lb)
D_{Fan} [cm]	154.9 (61.0 inch)	176.3 (69.4 inch)	325.1 (128.0 inch)
Non-chargeable TCLA*	10.2%	12.8%	9.4%
Chargeable TCLA*	6.2%	8.1%	5.5%
FAN η_p	0.904	0.914	0.916
LPC η_p	0.890	0.908	0.908
HPC η_p	0.880	0.893	0.902
HPT η_p^{**}	0.875	0.881	0.896
LPT η_p	0.889	0.900	0.905

Results are for aerodynamic design point (ADP) if not mentioned otherwise.
*TCLA shown is % relative to primary airflow.
**HPT η_p is cooled efficiency.

Engine "A" is a CFM56-7B-like engine installed on a B737-800 airframe. Engine "B" is a LEAP-1B-like engine installed on the same airframe, which represents a modern single-aisle engine with an increase in OPR, a decrease in FPR (i.e., increases

in BPR and fan diameter), along with an increase in TET and η_p. Finally, engine "C" is a GE90-115B-like engine installed on a B777-300ER airframe, representing a technology level in between engine "A" and engine "B", with a higher thrust category utilized for large twin-aisle, long-haul aircraft. Together, these three engine-aircraft combinations represent a wide range of current-day aviation, in that it includes single-aisle fleets with current/new engine options and actively operated long-haul fleet category.

In Figure 3-1, thrust-fuel flow result comparisons to the EDB data [34] are shown, where the relative RMS errors are within 2.5%.
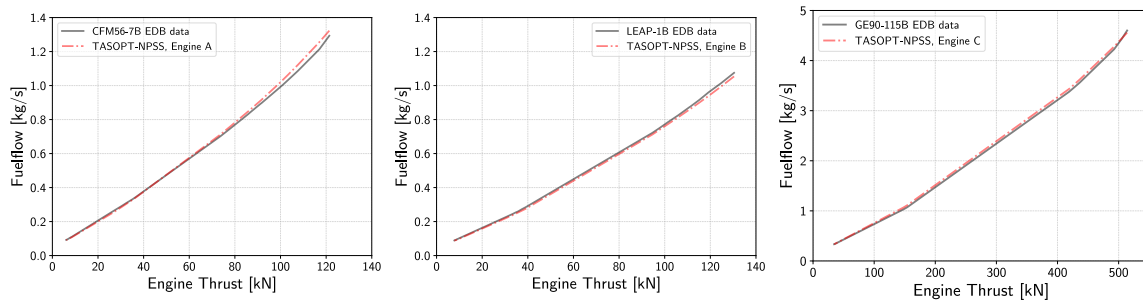
Figure 3-1: Thrust (SLS, uninstalled)-fuel flow comparison with ICAO EDB [34], for engine "A" (left), "B" (mid), "C" (right).

In Figure 3-2, the geometries of the three "designed" aircraft are shown, closely resembling the corresponding reference aircraft.
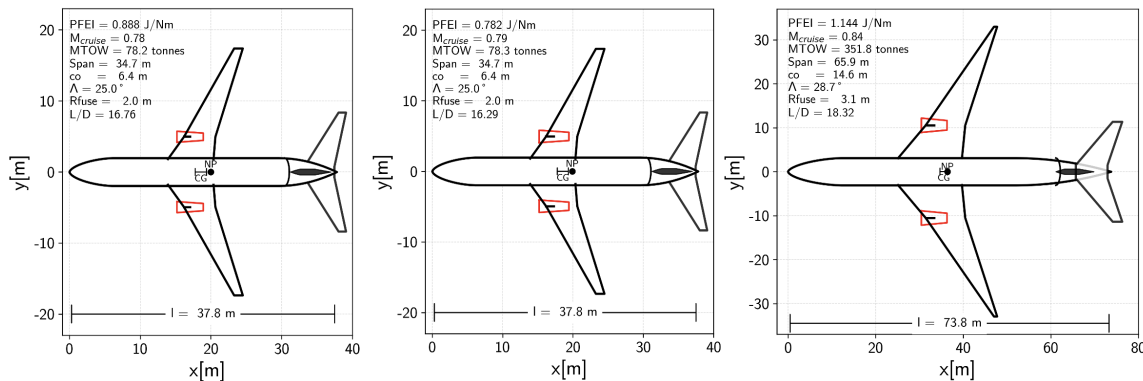
Figure 3-2: Top-down view and aircraft parameters for engine "A" (left), "B" (mid), "C" (right) installed aircraft models. PFEI values displayed are for max range MTOW mission (corresponding to point B in Figure 2-2).

In Figure 3-3, we present the weight and drag breakdown of the aircraft models. Aircraft's OEW, MTOW, payload, and maximum fuel capacity, closely match the publicly available data.
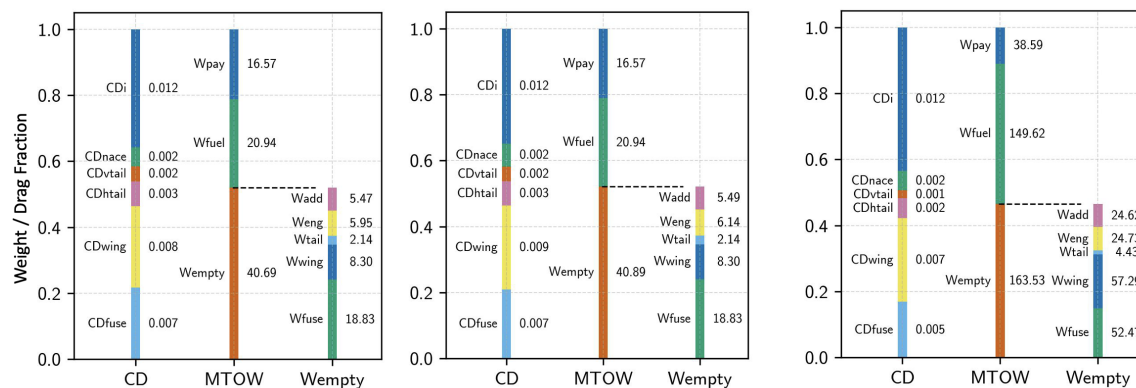
Figure 3-3: Weight and drag fraction breakdown for engine "A" (left), "B" (mid), "C" (right) installed aircraft models.

3.2 Baseline Engine Environmental Performance

We run "Aircraft-Engine-Fuel-Operations" scenarios for the three baseline engines using 2019 global fleet data. Full-fleet/full-flight emissions are calculated, with climate and air quality models used to obtain the global average temperature increase and human health impacts due to air quality degradation. These impacts are then monetized to obtain the NPV of climate and air quality costs.

In Table 3.2, we present the performance metrics for the baseline design of each engine. We show CO_2, NO_x, environmental cost (climate, air quality, and total), with each performance metric normalized with Revenue-Tonne-Kilometer (RTK). RTK is a suitable normalization factor as it reflects the actual productivity and is also applicable to cargo flights, including increasingly important belly cargo. This enables us to systematically compare the relative costs and benefits of each baseline engine and compare between different aircraft categories, such as B777-300ER (engine "C") and B737-800 (engines "A" and "B"). For NO_x, we also present D_p/F_{00}, which is the total NO_x emissions emitted during the LTO cycle relative to the rated thrust per ICAO Annex 16 Volume II [58], and $EI(NO_x)$ (block-average, LTO, climb, cruise).

Table 3.2: Baseline engine performance metrics.

Engine	"A"	"B"	"C"
CO_2/RTK [a] $\left[\frac{\text{gCO}_2}{(\text{Tonne}\cdot\text{km})}\right]$	795.9	710.3	674.5
NO_x/RTK $\left[\frac{\text{gNO}_x}{(\text{Tonne}\cdot\text{km})}\right]$	2.83	2.77 (2.15, 3.39) [b]	4.35
D_p/F_{00} NO_x [g/kN]	36.7	48.5	55.7
Avg. Block $EI(NO_x)$ $\left[\frac{\text{g-NO}_x}{\text{kg-fuel}}\right]$	11.2	12.3 (9.5, 15.1) [b]	20.4
LTO $EI(NO_x)$ $\left[\frac{\text{g-NO}_x}{\text{kg-fuel}}\right]$	10.7	19.4 (19.4, 19.4) [b]	25.1
Climb $EI(NO_x)$ $\left[\frac{\text{g-NO}_x}{\text{kg-fuel}}\right]$	14.5	16.2 (15.6, 16.8) [b]	29.0
Cruise $EI(NO_x)$ $\left[\frac{\text{g-NO}_x}{\text{kg-fuel}}\right]$	10.1	9.2 (4.6, 13.8) [b]	19.6
NPV_Climate/RTK [c] $\left[\frac{\$}{(\text{Tonne}\cdot\text{km})}\right]$	0.196 (0.0553, 0.453) [d]	0.181 (0.0507, 0.418) [d]	0.122 (0.0350, 0.276) [d]
$NPV_\text{Air Quality}$/RTK $\left[\frac{\$}{(\text{Tonne}\cdot\text{km})}\right]$	0.167 (0.0253, 0.389) [d]	0.159 (0.0244, 0.374) [d]	0.228 (0.0348, 0.538) [d]
NPV_Total/RTK [c] $\left[\frac{\$}{(\text{Tonne}\cdot\text{km})}\right]$	0.361 (0.137, 0.687) [d]	0.340 (0.128, 0.646) [d]	0.348 (0.118, 0.683) [d]

Weight load factor of 70% with respect to maximum payload is assumed
[a] Note that above CO_2/RTK is for direct combustion emissions (tank-to-wake, TTW)
[b] For engine "B" $EI(NO_x)$, low and high NO_x cases as shown in Figure 1 are provided in brackets.
[c] Climate impact assessment includes well-to-tank (WTK) emissions (CO_2e)
[d] For NPV/RTK, 5th and 95th percentile are provided in brackets.

Engine "B" shows an improvement in CO_2/RTK (i.e., fuel consumption) compared to engine "A", owing to higher cycle efficiencies and a lower FPR. Engine "C" has a lower CO_2/RTK compared to "A" and "B" primarily due to its high payload capacity and long-haul operations. We also observe different NO_x characteristics across the engines. Compared to engine "A", engine "B" has a higher OPR which leads to increased combustion temperatures. However with a cruise-NO_x optimized staged lean-burn combuster in engine "B", the $EI(NO_x)$ increase is limited to LTO and climb (high thrusts) with cruise $EI(NO_x)$ mitigated, resulting in a moderate increase in average block $EI(NO_x)$. Engine "C", equipped with conventional RQL combustors like engine "A", exhibits significantly higher $EI(NO_x)$ compared to engine "A" due to a higher OPR.

The D_p/F_{00} NO_x results for the three engines are compared with the NO_x/RTK results. Comparing engine "C" to "A", we observe a similar relative increase in NO_x/RTK and D_p/F_{00}. However, comparing engine "A" and "B", NO_x/RTK for engine "B" reduced by 2% (for mid-NO_x curve) while D_p/F_{00} increased by 32%, indicating that D_p/F_{00} does not adequately represent the full-flight NO_x performance. This is primarily because the D_p/F_{00} metric is "unaware" of the low cruise NO_x emissions of engine "B". By deriving a metric incorporating a data point closer to

the cruise operating condition (between 30% and 85% F_{00}), a more accurate representation of full-flight NO_x emissions can be achieved. This necessitates addressing the existing data gap by adding a cruise representative certification point within the aforementioned range, also suggested in Miller et al. [74].

Note that for engine "B", most cruise operating conditions fall within the "uncertain" region, with 53% of block NO_x emissions attributed to this region (when computed with mid-NO_x curve in Figure 2-4). Therefore, we display $EI(NO_x)$ calculated with mid-NO_x along with the $EI(NO_x)$ calculated using low and high NO_x curves, which are indicated in brackets. Also, although we use P3T3 models derived using the $EI(NO_x)$ data from ICAO EDB [34], the D_p/F_{00} presented differs from the ICAO EDB values, as we calculate this using the F_{00} value required for MTOW take-off from the TASOPT aircraft model rather than reference engine's documented maximum rated thrust. This approach allows us to align the calculation more closely with the actual LTO cycle and ensures consistency with other metric calculations.

The climate cost is primarily influenced by CO_2 emissions and contrail-cirrus. Engine "C" has the lowest climate cost per RTK, from a lower CO_2/RTK but also from a lower contrail impact per RTK benefiting from its high payload capacity, as we assume contrail impacts to scale with flight distance. The air quality cost results mostly from NO_x emissions. Engine "C", despite having the lowest fuel burn per RTK, has a significantly higher air quality damage compared to engine "A" due to higher OPR and cycle temperatures, offsetting its low climate cost and leading to a moderate reduction in total environmental cost. Engine "B" results in the lowest air quality damage due moderate increase in $EI(NO_x)$, with the reduction in fuel burn proportionally higher than the increase in average block $EI(NO_x)$, driving it towards lowest total environmental cost per RTK.

The total environmental impact per RTK can be referred to as an "integrated environmental metric", incorporating both climate and air quality impacts.

$$\textbf{Integrated Environmental Metric} = \frac{\text{Total Environmental Cost}}{\text{Revenue-Tonne-Kilometer (RTK)}}$$

It is important to note that while the sensitivity calculations do not require normalization since they involve relative changes, this integrated environmental metric provides a useful basis for systematic comparison between different scenarios as it assesses the environmental impact relative to the productivity generated by aviation. It is capable of capturing sensitivities to different aircraft subsystems' design, such as the airframe, engine, fuel type, and operations. This metric provides a basis for incentivizing lower environmental impact, and can be included as part of the aircraft or engine specification, alongside existing metrics such as SFC, weight, durability, and noise. Additionally, it can inform regulatory policies to better reflect the actual environmental impact of aviation. Compared to relying solely on regulatory limits, this approach is more applicable to driving aviation sustainability.

3.3 Intermediate Climate and Air Quality Results

This section demonstrates the steps involved in assessing the climate and air quality impacts of a specific "Aircraft-Engine-Fuel-Operations" scenario. We present the results of engine "A", "B", and "C", installed in corresponding reference aircraft (Table 3.1), considering 2019 operations on fossil Jet-A fuel. We calculate and present intermediate results for the climate and air quality impacts.

3.3.1 Emissions

Figure 3-4 visualizes the global flight schedule for 2019, obtained from OAG [47], which is used to calculate the full-fleet/full-flight emissions.
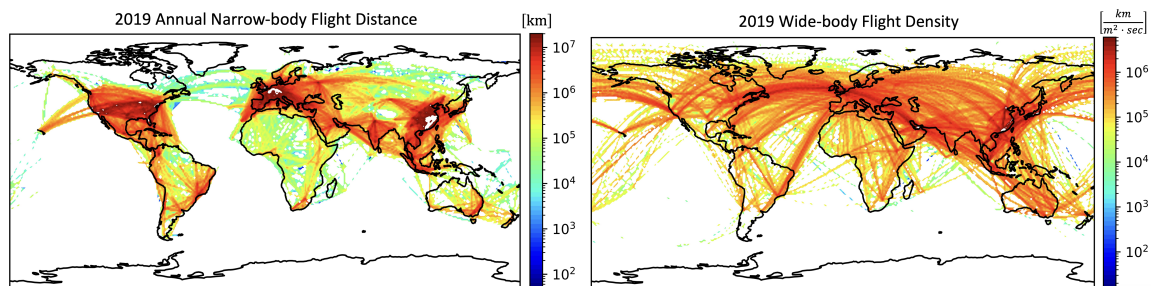
Figure 3-4: 2019 global schedule, for narrow-body (left) and wide-body fleet (right).

We can observe clear differences in flight distribution between the narrow-body fleet (for engines "A" and "B") and the wide-body fleet (for engine "C"). Emissions per RTK for the three engines are presented in Table 3.3.

Table 3.3: Emissions (g) per RTK for engines "A", "B", and "C".

Engine	CO_2	NO_x	CO	HC	Soot
"A"	795.9	2.83	0.893	0.120	9.51×10^{-3}
"B"	710.3	2.77	0.696	0.0362	4.67×10^{-4}
"C"	674.5	4.35	0.787	0.104	1.62×10^{-3}

* H_2O and SO_x emissions are calculated from fuel burn.

3.3.2 Climate Impact Results

Before moving onto the climate cost monetization, different intermediate climate impact results can be calculated. Results are normalized using a Revenue-Tonne-Kilometer (RTK) basis and calculated with a time horizon of 100 years.

First, RF-derived metrics such as AGWP, GWP, and CO_2e can be obtained. Absolute Global Warming Potential (AGWP) is defined as the integrated radiative forcing (RF) for a given time horizon (TH) due to unit mass of species X emitted:

$$\text{AGWP}_{\text{TH},X} = \int_0^{\text{TH}} \text{RF}_X dt$$

Global Warming Potential (GWP) is AGWP normalized using AGWP_{CO_2}, to show the relative radiative impact of species X relative to radiative impact of CO_2:

$$\text{GWP}_X = \frac{\text{AGWP}_X}{\text{AGWP}_{CO_2}}$$

Also, CO_2 equivalent, or CO_2e can be calculated using the GWP as:

$$\text{CO}_2\text{e} = \sum^X m_X \cdot \text{GWP}_X$$

AGWP_{100} and CO_2e per RTK are presented in Table 3.4. The variation between engines primarily stem from differences in fuel efficiency and contrail impacts. Fuel burn per RTK is the highest in engine "A", followed by engine "B" and engine "C" (see Table 3.2). In terms of contrail impact, which is assumed to scale with flight distance,

engines "A" and "B" are identical as they are assumed to operate under the same flight operations scenario (i.e., flight distances), with identical payload capabilities. Engine "C" exhibits lowest climate impact per RTK from both low fuel burn per RTK and low contrail impact per RTK, benefiting from high payload capacity.

Table 3.4: $AGWP_{100}$, CO_2e 100, and ATR_{100} per RTK for engines "A", "B", and "C".

Engine	$AGWP_{100}/RTK$ $\left[\frac{yr \cdot W/m^2}{Tonne \cdot km}\right]$	CO_2e $100/RTK$ $\left[\frac{gCO_2e}{Tonne \cdot km}\right]$	ATR_{100}/RTK $\left[\frac{deg}{Tonne \cdot km}\right]$
"A"	1.24×10^{-13}	1351	6.24×10^{-16}
"B"	1.01×10^{-13}	1258	5.79×10^{-16}
"C"	7.52×10^{-14}	770.7	3.70×10^{-16}

GWP_{100} for each emissions species is presented in Table 3.5. We can observe the relative climate forcing contributions of each emissions species, which exhibit variations across different engines, particularly in the case of NO_x, soot, and contrails.

Table 3.5: GWP_{100} for engines "A", "B", and "C".

Engine	CO_2	NO_x	Contrail -cirrus	H_2O	Soot	Sulfates	Total
"A"	1	-0.0335	0.649	$+0.0278$	$+0.0161$	-0.0945	$+1.565$
"B"	1	-0.0368	0.727	$+0.0278$	$+0.000882$	-0.0945	$+1.625$
"C"	1	-0.0607	0.240	$+0.0278$	$+0.00322$	-0.0945	$+1.116$

We can also obtain metrics related to global temperature change. AGTP, or the Absolute Global Temperature Potential, is a change in surface temperature ($\Delta T(t)$) at a given time t due to 1 kg of climate forcer emitted.

$$AGTP_X = \Delta T(t)$$

Global Temperature Potential (GTP) shows the temperature response due to emission species X compared to the temperature response from same mass of CO_2. GTP can be calculated by normalizing the $AGTP_X$ with the AGTP of CO_2, as below.

$$GTP_X = \frac{AGTP_X}{AGTP_{CO_2}}$$

AGTP and GTP for engine "A", normalized using RTK, are presented in Figure 3-5, where we see the climate impact timescales of short-lived forcers relative to CO_2.
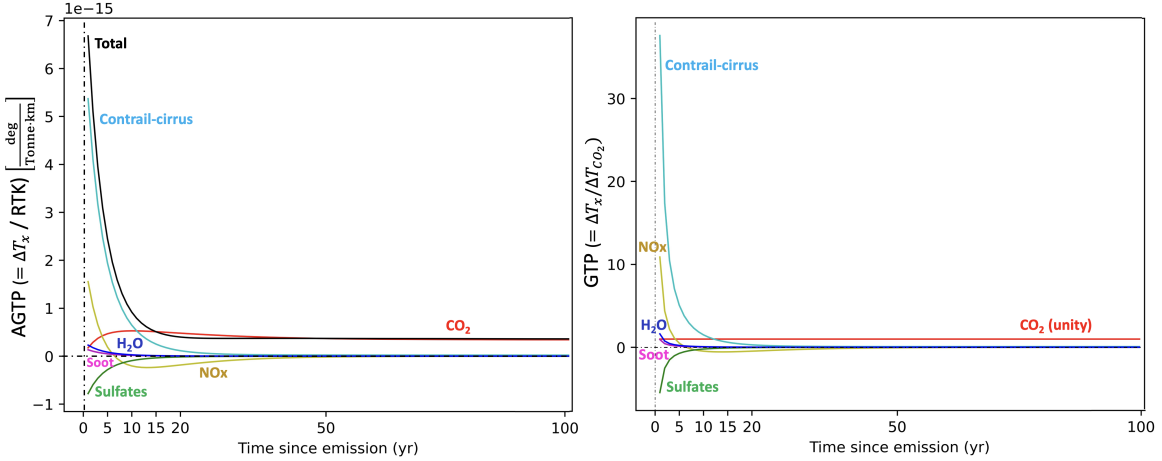
Figure 3-5: AGTP/RTK (left) and GTP (right) for engine "A".

Lastly, ATR_{100}, or Average Temperature Response per RTK is presented in Table 3.4. ATR is obtained by integrating the total ATP over a given time horizon, which is then averaged over the time horizon.

$$ATR = \frac{1}{TH} \int_0^{TH} AGTP\, dt$$

Lastly, we show the climate damage incurring due to 2019 engine "A" operation. Damage before discounting has a peak in the year of emission, then drops as effects from short-lived forcers decline, and then increases in a linear trend largely due to a near constant ΔT from the remaining CO_2 concentration and a linear GDP growth projection from the SSP2 scenario. Discounting is done using a discount rate of 3%.
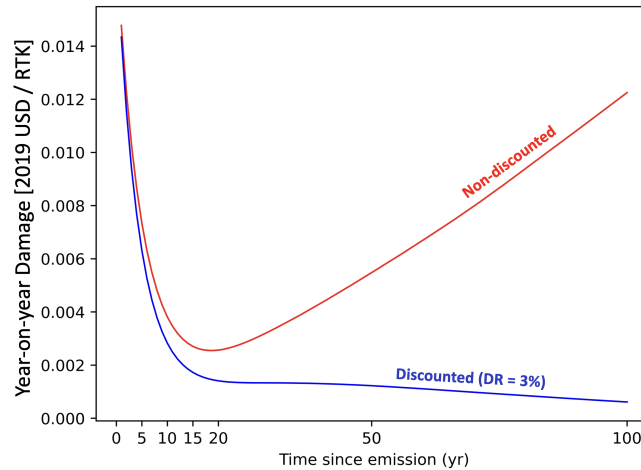
Figure 3-6: Climate damage per RTK for engine "A".

49

3.3.3 Air Quality Impact Results

The contribution of each emission species to increase in annual-average population-weighted ground-level O_3 and $PM_{2.5}$ exposure per RTK are presented in Table 3.6. Also, premature mortalities per RTK are presented in Table 3.7.

Table 3.6: Increase in annual-average population-weighted ground-level O_3 and $PM_{2.5}$ exposure per RTK, for engine "A".

	O_3 (MDA8) $\left[\frac{\text{ppbv}}{\text{Tonne·km}}\right]$	$PM_{2.5}$ $\left[\frac{\text{μg/m}^3}{\text{Tonne·km}}\right]$
NO_x	4.50×10^{-13}	4.94×10^{-14}
SO_x	1.16×10^{-14}	6.03×10^{-15}
BC	0	1.92×10^{-16}
HC	3.68×10^{-15}	2.89×10^{-16}
CO	2.92×10^{-15}	3.02×10^{-17}
OC	0	1.29×10^{-16}
Total	4.68×10^{-13}	5.61×10^{-14}

Table 3.7: Premature mortalities per RTK for engines "A", "B", and "C".

Engine	From O_3 (MDA8)	From $PM_{2.5}$	Total
"A"	1.74×10^{-8}	8.69×10^{-9}	2.61×10^{-8}
"B"	1.63×10^{-8}	8.80×10^{-9}	2.51×10^{-8}
"C"	2.51×10^{-8}	1.08×10^{-8}	3.59×10^{-8}

Chapter 4

Sensitivity to Engine Design Parameters

The "Engine Environmental Impact" (EEI) framework is used to calculate the sensitivity of aviation environmental impacts to engine design parameters. For the presented results, we first show the sensitivities of fleetwide block fuel consumption and fleetwide NO_x emissions to each parameter. These quantities are directly associated with the environmental impact (fuel burn or CO_2 emissions for climate impact and NO_x emissions for air quality impacts. Additionally, we compute sensitivities for climate and air quality impacts and the resulting total environmental impact, which is the sum of these two components.

To quantify environmental performance metric's sensitivity to engine design parameters, we conduct an engine design tradeoff study assuming that the aircraft parameters except for the engine are fixed. Note that this sensitivity, calculated using a central finite difference method varying each parameter by $\pm0.5\%$, is "local" to the baseline engine. Hence, if the relationship is not linear or there are tradeoffs that may result in a non-monotonic trend, a wider range must be investigated. Sensitivities are derived as non-dimensional influence coefficients, representing the fractional change in environmental performance metrics per fractional change in engine parameters. A positive sensitivity indicates that an increase in a parameter leads to more environmental damage, and vice versa. This environmental impact sensitivity to engine

design parameter i can be decomposed into two components: (1) the sensitivity of environmental impact to each emissions species j, and (2) the sensitivity of emissions to each engine design parameter, which can be expressed as follows:

$$\boldsymbol{S}(\text{Env. Impact}, \text{Eng. Param}_i) \left[\frac{\%}{\%}\right] =$$
$$\sum_j \frac{\text{Env. Impact}}{(\text{Eng. Param})_i} \left\{ \frac{\partial(\text{Env. Impact})}{\partial(\text{Emission})_j} \frac{\partial(\text{Emission})_j}{\partial(\text{Eng. Param})_i} \right\}$$

where the notation $\boldsymbol{S}(y, x)$ is defined as the normalized sensitivity of y with respect to x (percentage change in y resulting from a percentage change in x).

4.1   Sensitivity to Primary Cycle Design Parameters

4.1.1   Overall Pressure Ratio (OPR)

We present the environmental performance metric sensitivities to overall pressure ratio (OPR). For the three baseline engines, Table 4.1 shows a single point evaluation of fuel flow and NO_x emission rate sensitivities to OPR, for ADP and mid-cruise. We also present the sensitivity of D_p/F_{00} NO_x with respect to OPR to determine if this metric sufficiently captures the full-fleet/full-flight NO_x emissions trend.

Table 4.1:   Sensitivities [%/%] of fuel flow and NO_x emission rates at ADP and mid-cruise, and D_p/F_{00} NO_x, with respect to change in OPR.

Engine	$\dot{m}_{f.\mathrm{ADP}}$	$\dot{m}_{f.\mathrm{CRZ}}$ *	$\dot{m}_{\mathrm{NO}_x.\mathrm{ADP}}$	$\dot{m}_{\mathrm{NO}_x.\mathrm{CRZ}}$ *	D_p/F_{00} NO_x
"A"	-0.0707	-0.0461	$+0.797$	$+0.714$	$+1.22$
"B"	$+0.0234$	$+0.0515$	$+2.20$	$+1.71$	$+4.40$
"C"	-0.0485	-0.0131	$+1.11$	$+0.902$	$+1.72$

*Cruise fuel flow ($\dot{m}_{f.\mathrm{CRZ}}$) and cruise NO_x emission rate ($\dot{m}_{\mathrm{NO}_x.\mathrm{CRZ}}$) sensitivities are for mid-cruise

Table 4.2 and Figure 4-1 show the full-fleet/full-flight environmental performance metric sensitivities to OPR.

Table 4.2:   Sensitivities [%/%] of environmental performance metrics to OPR.

Engine	Fleet Fuelburn	Climate Cost	Fleet NO_x	Air Quality Cost	Total Env. Cost
"A"	-0.0526	-0.0728	$+0.932$	$+0.881$	$+0.358$
"B"	$+0.0594$	-0.0695	$+2.58$	$+2.37$	$+1.052$
"C"	-0.0108	-0.110	$+1.02$	$+0.990$	$+0.563$
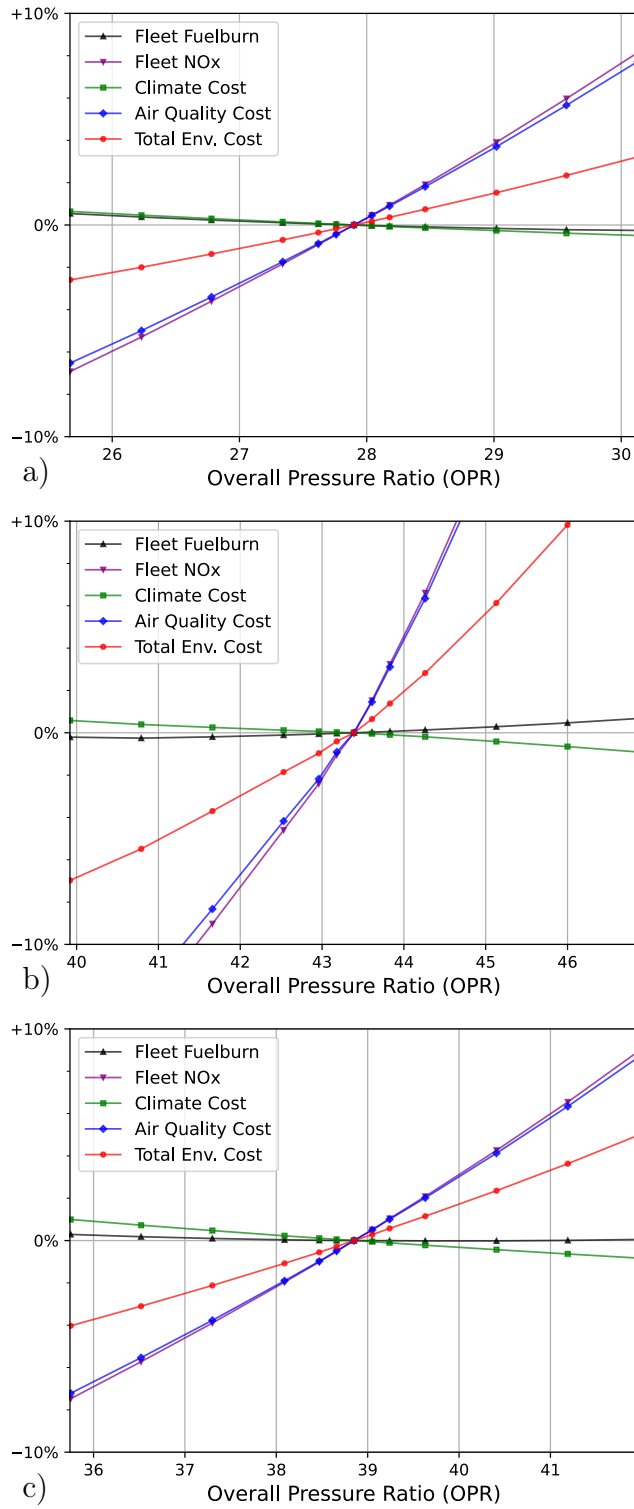
Figure 4-1: Performance metric change for change in Overall Pressure Ratio (OPR) for engine "A" (a), "B" (b), "C" (c).

Increasing the OPR generally improves cycle efficiency until a certain point (for a given TET), but it is also associated with an increase in NO_x emissions. Engines "A" and "C" show a fuel burn benefit from a further increase in OPR, for both the fleetwide results (Table 4.2) and the analyzed operating points (Table 4.1). Sensitivity values are higher for engine "A" due to its relatively low baseline OPR. Engine "B" results in a fuel burn penalty from a further increase in OPR. However, figure 4-1 illustrates that the design OPR for all of these cycles are located near the fuel-optimal OPR, assuming a fixed design TET and component efficiencies. Furthermore, as shown in Table 4.1, all three engines exhibit a stronger preference towards higher OPR at ADP compared to mid-cruise.

These analyses show that (1) fuel burn improvements from higher OPR are marginal, especially in fleet fuel burn sense; (2) further increasing pressure ratios on modern high OPR engines ("B") do not provide further fleet fuel burn benefit; (3) at part-power conditions, the advantages of a higher OPR are less notable because the efficiency gains are not significant enough to compensate for the increased engine weight and cooling requirements from higher temperatures of compressor extracted coolant gas.

While a further increase in OPR has a marginal impact on fuel burn, it leads to a significant increase in NO_x emissions due to higher temperatures in the combustion process. Fleetwide NO_x emissions increase rapidly, roughly 1% per percent change in OPR for engines "A" and "C", which is a similar increase as found by Guynn et al. [48] where 40% increase in $EI(NO_x)$ was found when the design OPR was increased from 32 to 42. For engine "B", this OPR-NO_x sensitivity is notably higher, with a fleetwide increase of 2.6% in NO_x emissions per percent increase in OPR. As shown by the opposite sign in the sensitivity results for fuel burn and NO_x, OPR tradeoff is technically a CO_2-NO_x tradeoff, and we observe that a 1.8% reduction in fleet NO_x emissions can be traded for roughly 0.1% increase in fleet fuel burn for engine "A".

For all three engines, higher OPR leads to a decrease in climate costs primarily due to the associated increase in NO_x emissions, which has a net cooling effect. The reduction in overall climate impact from NO_x emissions is approximately 3.4% in terms of costs (NPV) and 2.1% in terms of GWP_{100}/RTK (Table 3.4). Given that

more than 90% of air quality impacts occurring due to NO_x emissions, air quality damages increase with higher OPR and the subsequent increase in NO_x emissions. Overall, total environmental cost sensitivities show higher OPR to result in higher total environmental costs, primarily driven by a substantial air quality impact from an increase in NO_x emissions which offsets the gain in fuel efficiency. This conclusion of "higher OPR leads to more environmental cost" is consistent across ranges of other discount rates (i.e., valuation choices), as shown in Table 5.1.

Lastly, we compare the D_p/F_{00} and full-fleet/full-flight NO_x emissions sensitivities to OPR. Engine "A" shows the smallest difference between the two sensitivities, with D_p/F_{00} sensitivity being 30% higher than that of fleet NO_x sensitivity. This is because the D_p/F_{00} metric includes taxi (7% F_{00}) and take-off (100% F_{00}) condition which have higher T_3-EI(NO_x) sensitivities (see Figure 2-3). For engine "C", the discrepancy between the two sensitivities is increased further, with the D_p/F_{00} sensitivity being 65% higher than that of fleet NO_x. This is because compared to engine "A", (1) T_3-EI(NO_x) sensitivities of 7% and 100% F_{00} points have increased more than that of the cruise conditions (Figure 2-3) and (2) engine "C" is operated on long-haul routes (Figure 3-4 and Figure 4-6), which makes the full-flight sensitivity reflect the cruise condition more and LTO condition less. Engine "B" exhibits the highest difference between the two sensitivities, with D_p/F_{00} sensitivity being 70% higher than that of fleet NO_x. This is primarily driven by the high T_3-EI(NO_x) sensitivity at 100% and 85% F_{00} (Figure 2-4), which is partly offset by its short-haul operations reflecting the LTO sensitivity more. We also observe that the fleet NO_x sensitivities fall between the cruise NO_x emission rate ($\dot{m}_{NO_x.CRZ}$) and the D_p/F_{00} sensitivities, with engines "A" and "B" exhibiting a higher inclination towards the D_p/F_{00} sensitivity compared to engine "C", mainly due to the relatively higher proportion of LTO emissions from their short-haul fleet operations. These findings support the need for representative cruise point emissions values to be reported and included in assessments. This can enable full-fleet/full-flight NO_x emissions calculation and its sensitivity to a certain engine design parameter to be represented by interpolating between the cruise condition and LTO D_p/F_{00} values using a suitable weighting factor based on fleet operations.

4.1.2 Fan Pressure Ratio (FPR)

Many studies have focused on fan pressure ratio (FPR) tradeoffs, evaluating fuel burn, NO_x, and noise impacts [45, 48–50]. As FPR is reduced, specific thrust decreases thereby increasing the propulsive efficiency. Consequently, fan diameter must be increased to produce the same thrust level. Table 4.3 and Figure 4-2 show the environmental performance metric sensitivities to FPR, for the three baseline engines.

Table 4.3: Sensitivities [%/%] of environmental performance metrics to FPR.

Engine	$\dot{m}_{f.\mathrm{CRZ}}$	Fleet Fuelburn	Climate Cost	Fleet NO_x	Air Quality Cost	Total Env. Cost
"A"	+0.208	+0.207	+0.134	+0.189	+0.193	+0.160
"B"	+0.0710	+0.0952	+0.0588	+0.0886	+0.0946	+0.0751
"C"	+0.125	+0.0793	+0.0678	+0.0497	+0.0544	+0.0595

*Cruise fuel flow ($\dot{m}_{f.\mathrm{CRZ}}$) sensitivity is for mid-cruise

Figure 4-2 shows convex curves for all three engines, with different fuel-optimum FPR locations. The fuel-optimum FPR exists as moving to a lower FPR (to the left) increases the fan size and results in an increase in engine weight and drag penalty, while moving to a higher FPR decreases propulsive efficiency. Engines "A" and "B" have fuel-optimum FPRs of 1.49 and 1.53, respectively, which is in line with Guynn et al. [50], where the fuel-optimum FPR was found to be approximately 1.5 for direct-drive engines on a single-aisle aircraft. Engine "C" has a fuel-optimum FPR of 1.55, which is relatively closer to its baseline FPR compared to engines "A" and "B". The higher baseline FPRs of engines "A" and "B" compared to their fuel-optimum FPRs can be primarily attributed to fan size restrictions from the low fuselage design of the installed aircraft (i.e., B737). It should be noted that secondary impacts such as ground clearance, landing gear length, or vertical tail area resizing are not accounted.

We observe that the engine weight and drag penalty from a fan size change strongly influences the FPR tradeoff. We find that a 10% increase in fan diameter due to FPR reduction leads to a $1.2 - 1.4\%$ increase in aircraft drag and a $0.7 - 1\%$ increase in aircraft empty weight. Guynn et al. [48–50] observed that updating the engine weight model resulted in a shift of the fuel-optimal FPR from 1.6 to 1.5, primarily driven by a decrease in weight penalty associated with a lower FPR (i.e., larger fan size). This shows that accurate models for estimating engine weight and drag are crucial for assessing the impact of FPR tradeoffs on aircraft performance.
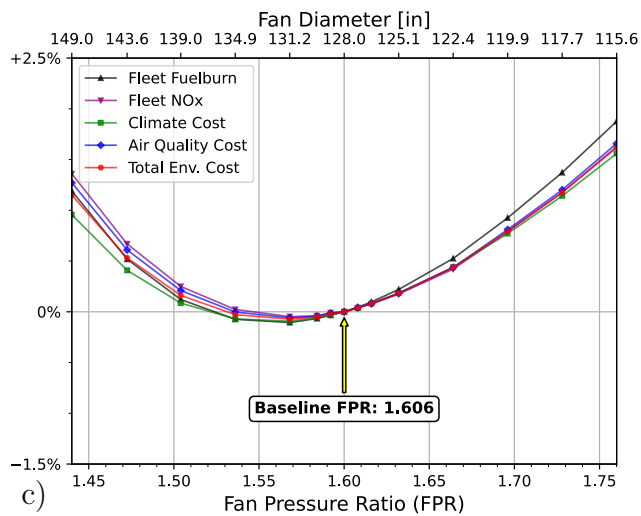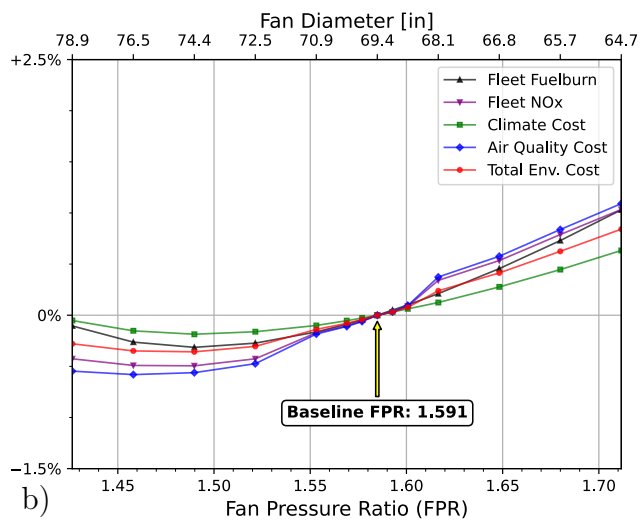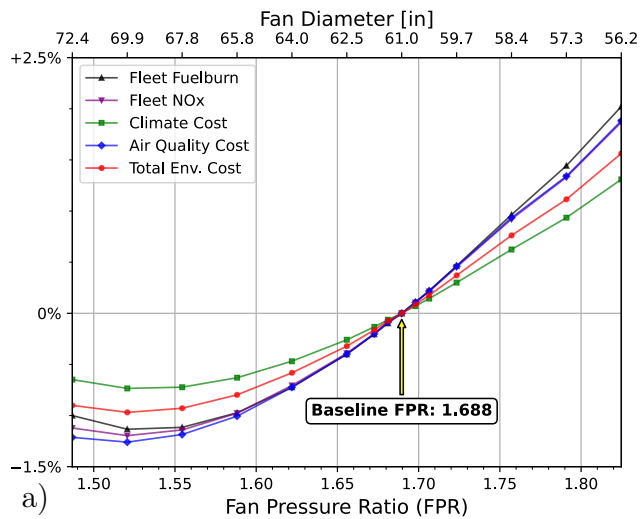
Figure 4-2: Performance metric change for change in Fan Pressure Ratio (FPR) for engine "A" (a), "B" (b), "C" (c).

The climate cost curves follow those of the fleet fuel burn, but they are less steep. This is mainly due to the impact of contrails on climate change, which accounts for approximately 40% of the total climate cost. As mentioned earlier, the contrail impact is assumed to scale with flight distance and therefore is not sensitive to changes in engine design. Therefore, the relative change in the climate cost is less than the relative change in fleet fuel burn (i.e., CO_2). Figure 4-2 shows this effect to be more pronounced in engines "A" and "B", where relative proportion of contrail impacts are higher than that of engine "C" as described in Section 3.2.

Fleet NO_x emissions follow the trend of fleet fuel burn, as the core design parameters and hence $EI(NO_x)$ remain largely unchanged. Since NO_x-induced $PM_{2.5}$ and O_3 are the dominant contributors to air quality impacts [46], air quality cost curves follow the NO_x emission curves. We assume that $T_{t4.ADP}$ remains constant, although other studies have utilized different assumptions resulting in different FPR-NO_x trends, such as in Guynn et al. [48–50] where $T_{t4.ADP}$ was raised for lower FPR to offset thrust lapse effects, resulting in increased block NO_x emission with lower FPR. We should note that the kinks observed in NO_x and air quality curves of engine "B" are due to assumed discontinuity in P3T3 NO_x emissions model (Figure 2-4).

The total environmental cost curve also follows the trend of fleet fuel burn, indicating that reducing FPR for engines "A" and "B" would be environmentally beneficial, while engine "C" is closer to the environmentally-optimal FPR. It is worth noting that this paper did not investigate the effects of reducing FPR on noise, but lower FPR can offer noise reduction due to lower jet noise and fan tip speed [45, 48–50].

The results presented in Figure 4-3 provide another interesting perspective of FPR tradeoff, specifically its dependence on mission range. Shorter missions are shown to have a higher preference of going to a lower FPR, as they spend most times in relatively low Mach regimes. This is because of thrust lapse, where engines with low FPR inherently experience greater loss of thrust with higher airspeed. For engine "C", however, we observe that its longer mission ranges begin to benefit from a reduction in cruise fuel consumption from a lower FPR. Results also show that there is a minimum fuel burn per RTK, which occurs at approximately half the design range.

This is because short-range missions are at a disadvantage as they spend less time in cruise segments, while long-range missions face a disadvantage as they consume more fuel to carry the higher fuel load. These analyses demonstrate the importance of using realistic fleet operational scenarios.
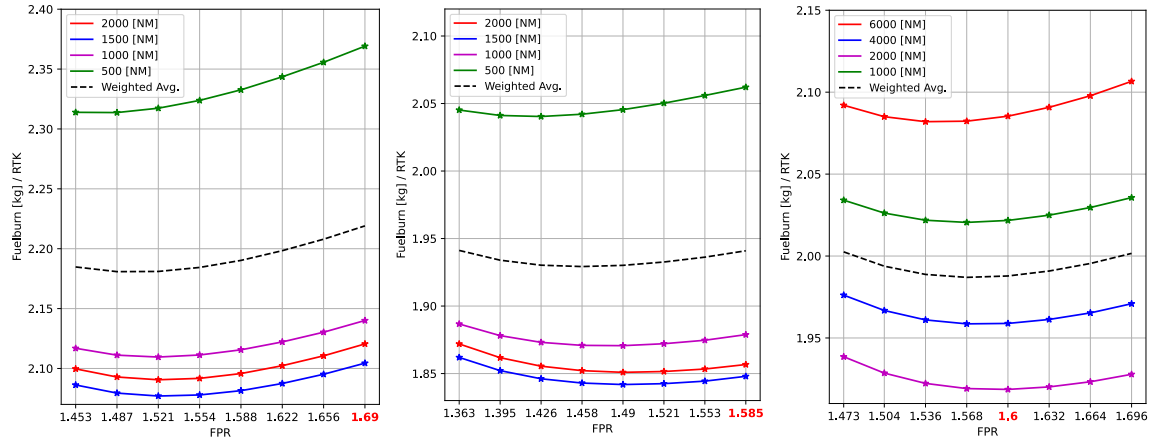
Figure 4-3: FPR-fuel burn tradeoff for different mission ranges for engine "A" (left), "B" (mid), "C" (right). Baseline design FPR (at ADP) annotated in bold red.

4.1.3 Turbine Entry Temperature (TET), T_{t4}

An increase in turbine entry temperature (TET), assuming a fixed ADP thrust requirement and fan size, results in a core size reduction ($\dot{m}_{core}$), leading to higher bypass ratios (BPR). Furthermore, to maintain a fixed limit of HPT blade metal temperature, a higher cooling flow is necessary, as illustrated in Figure 4-4.
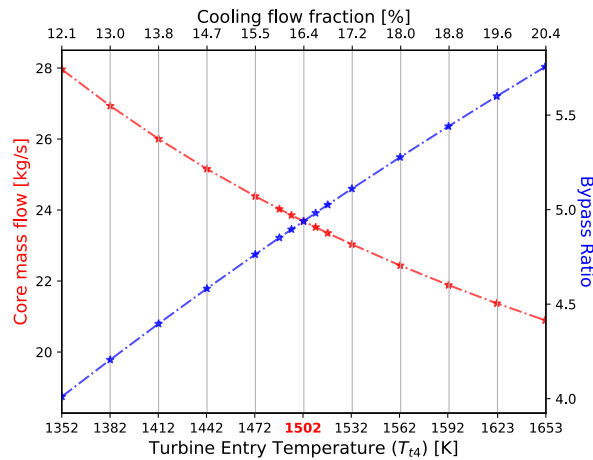
Figure 4-4: For engine "A", change in engine core size ($\dot{m}_{core}$ at ADP), bypass ratio, and cooling flow fraction with increasing TET. FPR and fan size are held constant.

Figure 4-5 demonstrates the existence of a fuel-optimum TET, as decreasing TET (moving to the left) results in a decrease in thermal efficiency, while increasing TET leads to increased cooling flow requirement and a consequent reduction in HPT efficiency. The convex shape of the curves in Figure 4-5 illustrates this tradeoff and indicates that the baseline designs of the three engines are located near the fuel-optimum T_{t4}. We can also observe that the change in climate cost is comparatively less than that of the fuel burn, as the contrail climate impact remains constant throughout TET variation. Again, this effect is more prominent in engines "A" and "B" due to their relatively higher proportion of contrail impact.

In Table 4.4, we observe that the difference between the mid-cruise and fleet fuel burn sensitivities is quite large. When examining the off-design performance of engines, we find that increasing the design TET with a fixed design OPR leads to greater fuel burn reductions for part-power conditions ($F_{\text{off-design}} < F_{\text{ADP}}$). A higher design TET, when coupled with a constant percentage reduction in thrust, results in a greater absolute temperature reduction. As a consequence, the thermodynamic cycle from station 3 to 4 follows a lower pressure isobar curve, which corresponds to a lower OPR indicating that the power required by the compressors are reduced. Therefore, when the design TET is increased, fuel consumption is reduced for off-design part-power conditions, with a higher relative reduction observed at lower power levels.

Table 4.4: Sensitivities [%/%] of environmental performance metrics to TET.

Engine	$\dot{m}_{f.\text{ADP}}$	$\dot{m}_{f.\text{CRZ}}$ *	Fleet Fuelburn	Climate Cost	Fleet NO$_x$	Air Quality Cost	Total Env. Cost
"A"	+0.0569	+0.0405	−0.000252	+0.00186	−0.0477	−0.0495	−0.0213
"B"	+0.0255	+0.0183	−0.0114	−0.00310	−0.104	−0.103	−0.0489
"C"	+0.0524	+0.0371	+0.0233	+0.0212	+0.000892	−0.0.000913	+0.00264

*Cruise fuel flow ($\dot{m}_{f.\text{CRZ}}$) sensitivity is for mid-cruise case

Table 4.5 presents fuel burn sensitivities to TET for different off-design operating points for engine "A". For ADP, we can observe that higher TET leads to higher fuel burn from as the influence of increased cooling flow and the associated HPT efficiency loss is greater than thermal efficiency gain. Lower-than-ADP thrust points (low-mass and mid-mass cruise) result in smaller increases in fuel consumption, whereas the higher-than-ADP thrust points (FL350 climb and mid-mass cruise) result in larger increases in fuel consumption, as explained above. Similarly, for sea-level static (SLS)
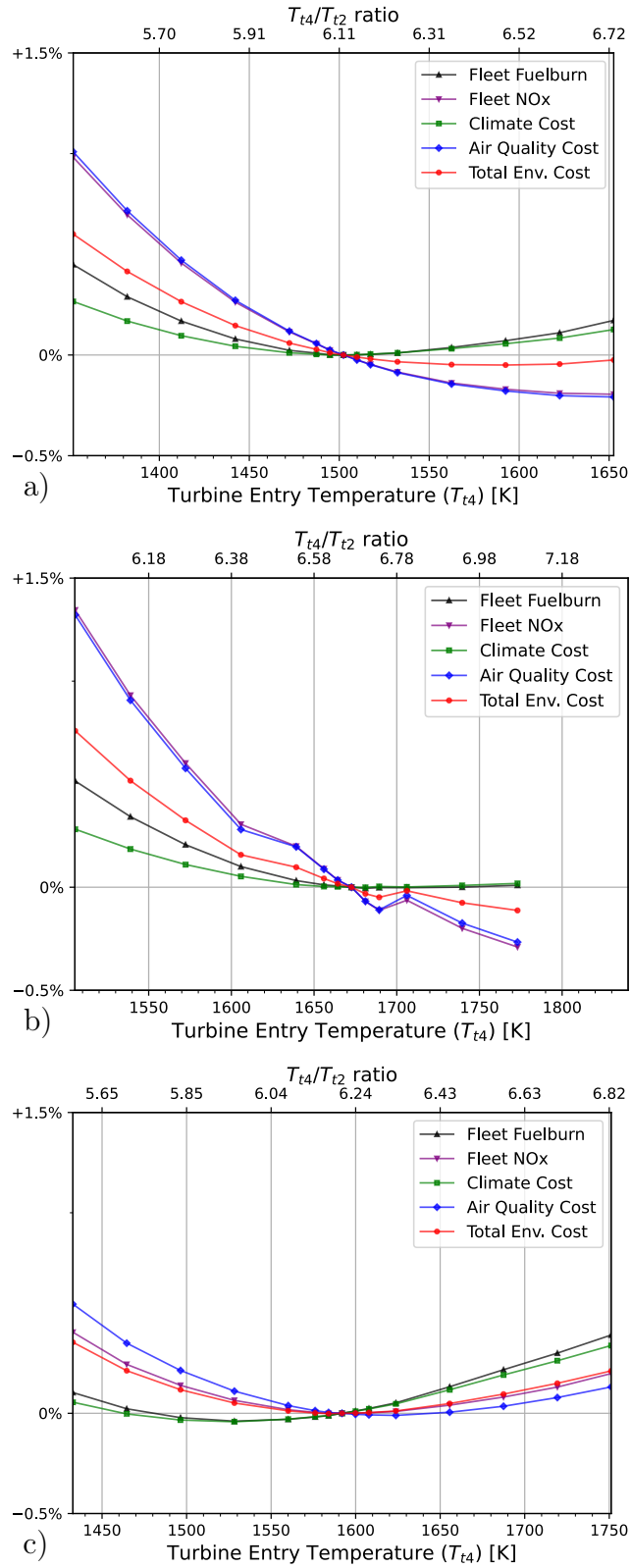
Figure 4-5: Performance metric change for change in Turbine Entry Temperature (TET) for engine "A" (a), "B" (b), "C" (c).

points used for LTO emissions calculations, lower thrust points exhibit significantly higher relative reductions in fuel burn from higher TET.

Table 4.5: Sensitivities [%/%] of fuel flow ($\dot{m}_f$) to TET, for ADP and different off-design operating conditions, for engine "A".

ADP	Climb FL350	Cruise High Mass	Cruise Mid Mass	Cruise Low Mass	SLS 100%	SLS 85%	SLS 30%	SLS 7%
+0.0569	+0.0889	+0.0568	+0.0405	+0.0123	+0.00382	−0.0221	−0.147	−0.282

Table 4.4 also highlights a significant differences between ADP and fleetwide fuel burn sensitivities for engines "A" and "B" compared to engine "C". This discrepancy arises from the fact that engines "A" and "B" are operated at a lower average thrust level compared to engine "C". The average thrust level can be determined by referencing the N1 spool speed in relation to N1 at ADP, which serves as the primary thrust reference variable. There are three main factors contributing to this observation. Firstly, engines "A" and "B" are flown on short-haul flights, as depicted in Figure 4-6. Consequently, a larger portion of their total flight time and emissions is attributed to descent and LTO operations, which include extended periods of low thrust during approach and taxi. Specifically, on engines "A" and "B", the LTO fuel burn accounts for approximately 11% of the total fuel burn, while for engine "C", it represents approximately 4.6% of the total fuel burn. Secondly, the nature of short-haul operations implies that engines "A" and "B" operate at a relatively lower power level during cruise due to lower aircraft mass level from smaller fuel load, resulting in engines "A" and "B" having more part-power operating conditions. Specifically, we find the average $(N1)_{CRZ}/(N1)_{ADP}$ to be 0.93 for engines "A" and "B", and 0.96 for engine "C". Lastly, the "size-within-family" effect plays a role. As indicated in Table 1, engines "A" and "B" are installed on a B737-800, which is a middle-of-family airframe within the Boeing 737NG and 737MAX family, whereas engine "C" is installed on a B777-300ER, which is the largest-of-family airframe among the B777-200LR/F variants. As we assume that each engine is installed on a single airframe for our fleet simulation, this leads to engines "A" and "B" being operated at a comparatively lower average N1, further deviating from the ADP value. Collectively, these three factors

contribute to engines "A" and "B" displaying a more pronounced shift in fleet fuel burn sensitivity towards part-power conditions.
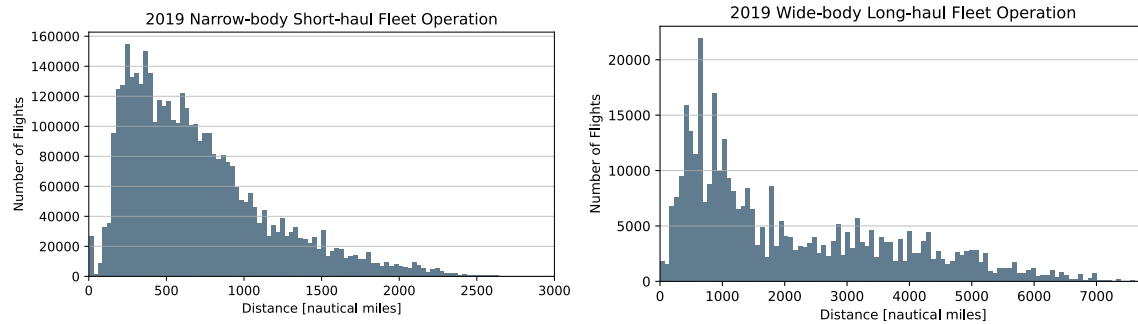
Figure 4-6: Fleet operation scenarios from 2019 OAG [47] for engines "A", "B" (left), and engine "C" (right).

For the NO_x emissions, Figure 4-5 shows the fleet NO_x emissions curve deviating from the fleet fuel burn curve. As OPR, T_3, and consequently the $EI(NO_x)$ remain constant at ADP, this indicates changes in off-design $EI(NO_x)$. As illustrated in the above fuel burn analyses, increasing the design TET leads to lower values of OPR for off-design part-power conditions. This leads to a decrease in $EI(NOx)$, as a lower OPR results in reduced values of P_3 and T_3. Hence, due to low power settings during descent and LTO, along with the average $(N1)_{CRZ}$ being lower than $(N1)_{ADP}$, we observe a decrease in $EI(NO_x)$ for higher TET and vice versa. This shifts the NO_x-optimal TET to be higher than the fuel-optimal TET. This effect is again greater for engines "A" and "B" compared to engine "C". However, the higher change in $EI(NO_x)$ observed for engine "B" compared to engine "A" is not due to larger off-design T_3 or OPR variations, but rather from higher T_3-$EI(NO_x)$ sensitivities for cruise and climb points, as shown in Figures 2-3 and 2-4. Note that for engine "B" (see Figure 4-5), higher design TETs beyond 1770K are not displayed as they do not meet takeoff thrust requirements, and the non-monotonic NO_x and air quality curves are again due to the assumed discontinuity in the P3T3 NO_x emissions model for the staged combustor.

We should underscore the importance of the impact of cooled HPT efficiency changes resulting from variations in cooling flow for this TET tradeoff. This is also true for any tradeoff that leads to a substantial change in cooling requirement. Figure

4-7 shows the case where we intentionally exclude the HPT efficiency change ($\Delta(\eta_p)$) resulting from the change in cooling fraction. This deliberate omission shows a notable difference compared to the actual tradeoff illustrated in Figure 4-5-(a), showing that all metrics continue to benefit from increasing TET without the existence of an optimal point.
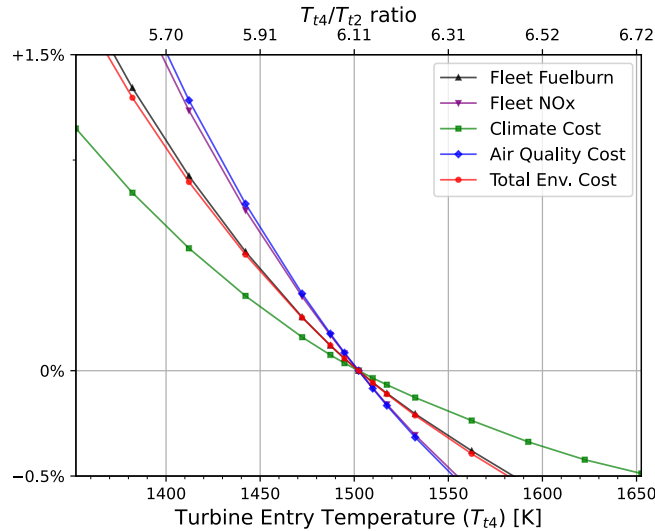
Figure 4-7: TET tradeoff for engine "A", when the cooled HPT η_p change from a change in cooling flow is not modeled.

Furthermore, it is important to consider that a higher TET can potentially have negative impacts on the hot section lifetime and maintenance costs, particularly at a fixed technology level. Moreover, an increase in TET can result in a reduction in core size, leading to a decrease in polytropic efficiency and may introduce manufacturing limitations, which could shift the fuel-optimum TET towards lower values. On the other hand, while we keep the engine weight constant for this tradeoff, core size (i.e., $\dot{m}_{\text{core}}$) reduction can lead to engine weight reduction, hence lower thrust requirements, potentially shifting the fuel-optimum TET towards higher values.

Overall, we find that it is important to conduct full-flight evaluations as even if a quantity remains constant at ADP, off-design variations can occur. Through the fuel burn and NO_x sensitivities (and consequent environmental impact sensitivities), we also find that fleet-wide analysis incorporating representative operation scenarios is important, which was also shown to be crucial for the FPR tradeoff.

64

4.2 Sensitivity to Secondary Cycle Parameters

4.2.1 Material Temperature Capability

Table 4.6 and Figure 4-8 show the sensitivity results for material temperature capability. We use the HPT blade metal temperature at rotation (end-of-runway) as a surrogate for material temperature capability. Higher material temperature capability results in less cooling air to be extracted from the compressor stages, leading to a reduction in engine's core size. This decrease in cooling flow extraction (i.e., less "wasted" work) and associated increase in HPT cooled efficiency results in fuel burn and climate cost reduction. Results show that the fuel burn sensitivities to material temperature capability are proportional to the baseline engine's cooling flow fraction (Table 3.1). Hence, engine "B" exhibits the highest fuel burn sensitivity to material temperature capability.

Table 4.6: Sensitivities [%/%] of environmental performance metric to material temperature capability.

Engine	$\dot{m}_{f.\mathrm{CRZ}}$	Fleet Fuelburn	Climate Cost	Fleet NO_x	Air Quality Cost	Total Env. Cost
"A"	-0.390	-0.620	-0.397	-0.652	-0.681	-0.524
"B"	-0.814	-1.22	-0.740	-1.41	-1.38	-1.03
"C"	-0.456	-0.619	-0.502	-0.665	-0.717	-0.633

*Cruise fuel flow ($\dot{m}_{f.\mathrm{CRZ}}$) sensitivity is for mid-cruise case

As material temperature capability increases, there is a reduction in fleet NO_x emissions and air quality costs. As OPR and TET are assumed fixed at ADP, EI(NO_x) also remains constant at ADP. However, the NO_x curves of all three engines are steeper than that of the fuel burn line, indicating a change in off-design EI(NO_x). This can be attributed to cooled turbine entry temperature ($T_{4.1}$) changing with cooling flow variation. As $T_{4.1}$ is the temperature at which work is extracted from, the off-design EI(NO_x) change and the differences in the magnitude of this behavior across the three engines can be explained using the same methodology as the TET tradeoff. Here, we again mention the significance of modeling the HPT efficiency drop associated with an increase in cooling flow, with the sensitivities (i.e., benefits of higher material temperature capability) underestimated by $30 - 40\%$ when this cooled efficiency change is not modeled.
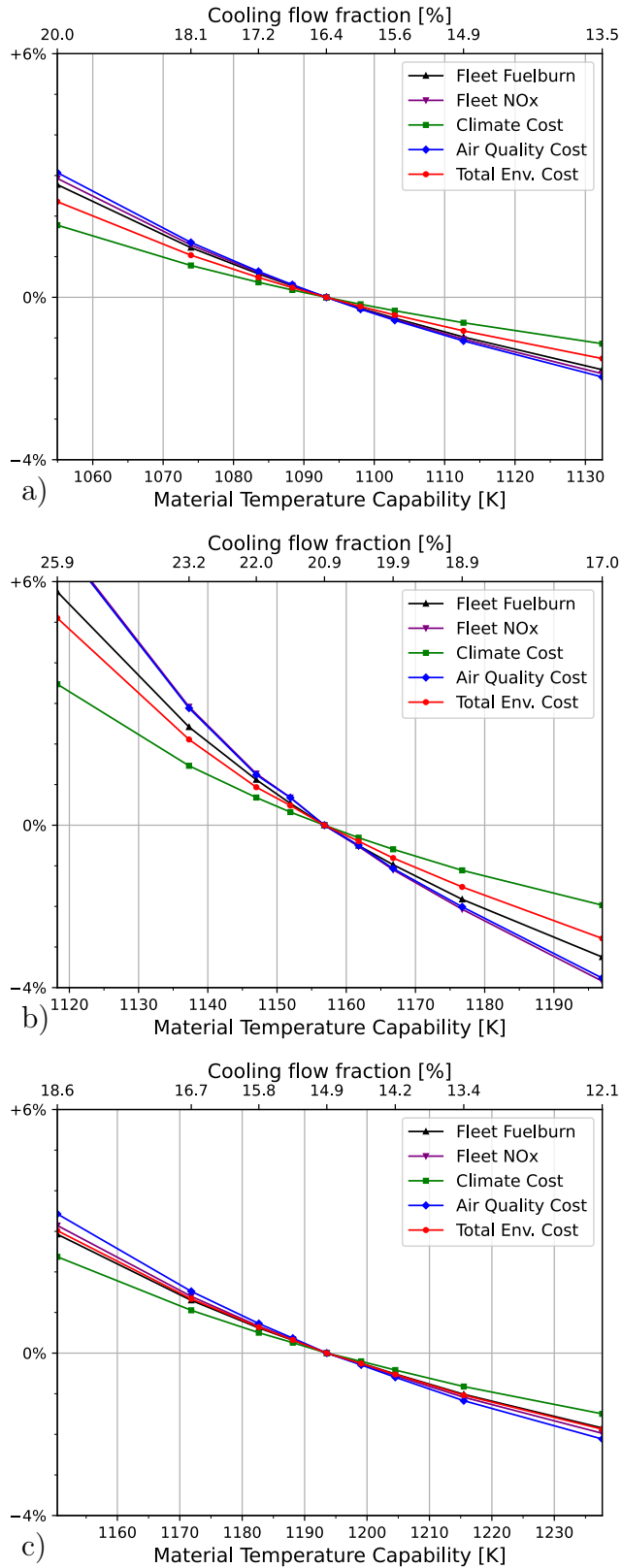
Figure 4-8: Performance metric change for change in material temperature capability for engine "A" (a), "B" (b), "C" (c).

4.2.2 Relative Cooling Flow (X_{cool})

Relative cooling flow, denoted as X_{cool}, is a non-dimensional cooling factor used to calculate the flow requirement of the coolant, as explained in Section 2.1.2. A higher X_{cool} indicates more cooling flow required to achieve a given amount of cooling. Note that X_{cool} for the first HPT vane row and all other turbine elements are increased or decreased by the same fractional quantity.

The relationship between X_{cool} and the material temperature capability is closely related, as both influence the engine performance by changing the cooling flow fraction, albeit with different scaling factors. Observing the cooling flow fraction change, we find that for all three engines analyzed, a 10K increase in material temperature capability is equivalent to reducing the X_{cool} by 6%.

Table 4.7 and Figure 4-9 show that higher X_{cool} (more cooling flow required) results in increased fuel burn, hence higher climate damage. NO_x emissions also increase primarily due to higher fuel burn, hence higher air quality damage. Total environmental cost has a positive sensitivity to X_{cool}, indicating that an improvement in cooling technologies (reducing X_{cool}) results in less environmental damage.

Table 4.7: Sensitivities [%/%] of environmental performance metric to X_{cool} (relative cooling flow).

Engine	$\dot{m}_{f.\text{CRZ}}$	Fleet Fuelburn	Climate Cost	Fleet NO_x	Air Quality Cost	Total Env. Cost
"A"	+0.0603	+0.0846	+0.0542	+0.0897	+0.0938	+0.0719
"B"	+0.105	+0.139	+0.0841	+0.174	+0.174	+0.125
"C"	+0.0647	+0.0828	+0.0671	+0.0895	+0.0963	+0.0849

*Cruise fuel flow ($\dot{m}_{f.\text{CRZ}}$) sensitivity is for mid-cruise case

The calculated sensitivities to material temperature capability and relative cooling flow (X_{cool}) are in line with those reported in the literature. Wilcock et al. [98] calculated sensitivities for general gas turbines with cycle parameters similar to engine "A", and reported a fuel burn reduction of 0.417 [%/%] for material temperature capability and 0.0612 [%/%] for cooling effectiveness improvement. Wilfert et al. [99] reported an SFC improvement of approximately 0.06 [%/%] for lower cooling air extracted. Our findings for engine "A" are comparable in scale with the these two studies, with an ADP fuel burn reduction of 0.354 [%/%] for higher material
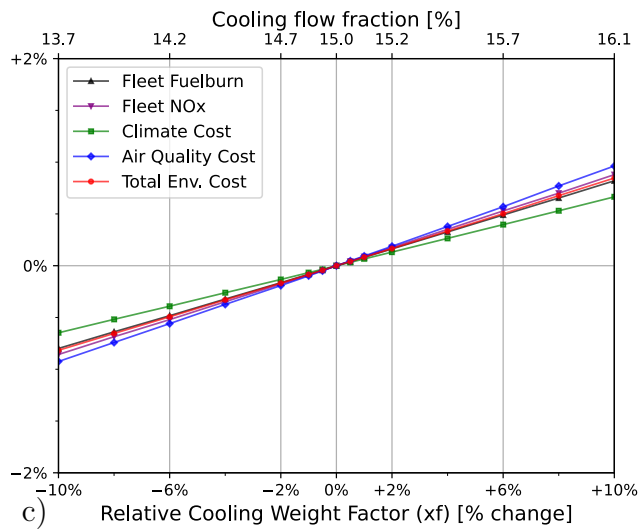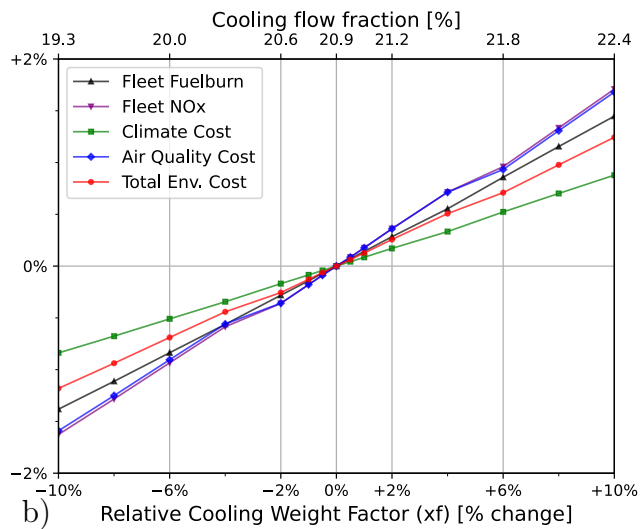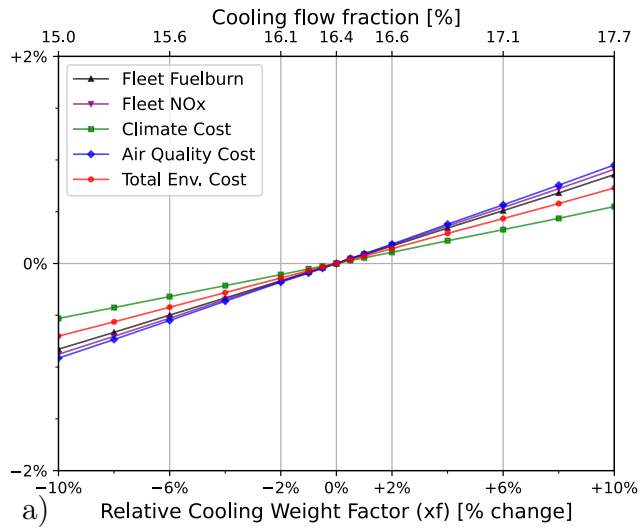
Figure 4-9: Performance metric change from change in relative cooling flow (X_{cool}) for engine "A" (a), "B" (b), "C" (c).

temperature capability and 0.0547 [%/%] for less cooling air extracted. Cumpsty [20] showed a design point fuel burn reduction of 0.0322 [%/%] for HPT cooling flow reduction for an engine similar to engine "C", while we find an ADP fuel burn reduction of 0.0610 [%/%] for engine "C". This gap may originate from different HPT η_p drop or ADP cooling assumptions (Cumpsty assumed 5% while we assume 15% of core flow).

Similar to TET and material temperature capability tradeoffs, we find the significance of modeling the change in HPT η_p with cooling fraction variations, with sensitivities underestimated by $30-45\%$ neglecting the drop in HPT cooled efficiency.

4.3 Sensitivity to Turbomachinery Component Polytropic Efficiency (η_p)

We examine the sensitivities of environmental metrics to turbomachinery component efficiencies. Sensitivities to component efficiencies presented in Table 4.8 and Figure 4-10 are derived as relative percentage change in each metric to an absolute percentage point change in polytropic efficiency (η_p). Note that this is assuming a change in η_p at design stage, rather than an assessment of a degradation of an engine-in-operation.

Table 4.8: Sensitivities [%/%] of environmental performance metric to turbomachinery component polytropic efficiencies (η_p), for each engine.

η_p	Engine	$\dot{m}_{f,\text{CRZ}}$	Fleet Fuelburn	Climate Cost	Fleet NO$_x$	Air Quality Cost	Total Env. Cost
FAN	"A"	-0.499	-0.555	-0.355	-0.607	-0.603	-0.466
	"B"	-0.772	-0.807	-0.489	-0.961	-0.954	-0.701
	"C"	-0.612	-0.712	-0.575	-0.782	-0.797	-0.710
LPC	"A"	-0.406	-0.503	-0.295	-1.22	-1.20	-0.702
	"B"	-0.343	-0.371	-0.187	-1.35	-1.07	-0.592
	"C"	-0.209	-0.253	-0.166	-0.676	-0.675	-0.477
HPC	"A"	-0.843	-1.10	-0.648	-2.61	-2.60	-1.53
	"B"	-1.39	-1.76	-0.761	-9.42	-8.78	-4.45
	"C"	-1.06	-1.30	-0.847	-3.47	-3.51	-2.48
HPT	"A"	-0.580	-0.747	-0.480	-0.769	-0.798	-0.621
	"B"	-0.744	-0.926	-0.560	-1.13	-1.13	-0.819
	"C"	-0.654	-0.801	-0.651	-0.852	-0.909	-0.808
LPT	"A"	-0.685	-0.745	-0.478	-0.803	-0.800	-0.621
	"B"	-0.808	-0.825	-0.503	-0.931	-0.928	-0.697
	"C"	-0.656	-0.756	-0.613	-0.819	-0.832	-0.746

*Cruise fuel flow $(\dot{m}_{f,\text{CRZ}})$ sensitivity is for mid-cruise case

For all three engines, HPC η_p exhibits the largest sensitivity for all shown metrics. For fan/HPT/LPT η_p improvement, NO_x and air quality cost reductions are almost solely attributable to the fuel burn reduction. However, for LPC and HPC, improvement in η_p is directly related to $EI(NO_x)$, as higher efficiency corresponds to smaller temperature rise (lower T_{t3}) for a given pressure ratio. Therefore, the total effect of fleet NO_x reduction for LPC and HPC efficiency improvements is a combination of effects from lower T_{t3} plus a fuel burn benefit.
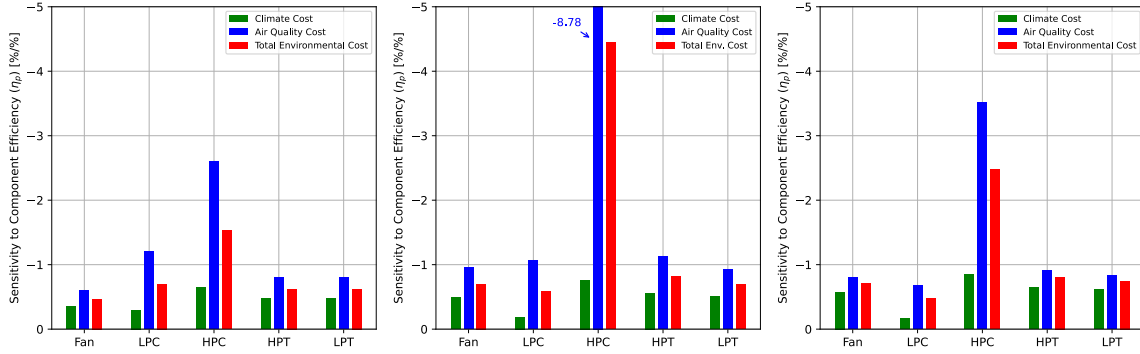
Figure 4-10: Sensitivities [%/%] of climate, air quality, and total environmental cost to turbomachinery component efficiency for engine "A" (left), "B" (mid), "C" (right).

Percentage changes in cruise SFC from η_p change shown in Table 4.7 are compared with Cumpsty [20] and Cumpsty and Heyes [21], who studied the effect of design point variation of component polytropic efficiencies on two reference engines. Cruise SFC sensitivities to fan, LPC, HPC, HPT, LPT η_p were 0.63, 0.36, 1.13, 0.69, 0.66 [%/%] for an engine with FPR 1.65, OPR 40, TET 1450K [20], and 0.88, 0.29, 0.87, 0.58, 0.86 [%/%] for an engine with FPR 1.5, OPR 45, $T_{t4}/T_{t2} = 6.11$ [21]. Results are in good agreement in that each η_p influence is proportional to the work done or extracted by the component, HPC η_p shows a high sensitivity while LPC η_p shows a low sensitivity, HPT and LPT sensitivities are similar, and fan η_p sensitivity increases for lower FPR (i.e., higher BPR) engine. Sensitivities to η_p are higher than material temperature capability and higher than that of X_cool, consistent with Wilcock et al. [98].

4.4 Sensitivity to Engine Weight

With total engine weight accounting for approximately 15% of aircraft empty weight, engine weight saving is directly related to aircraft performance. Engine weight savings can be obtained through use of advanced materials/manufacturing methods such as composites and additive manufacturing, or advanced analysis methods to optimize structural weights.

Table 4.9 and Figure 4-11 illustrate the sensitivities of environmental metrics to changes in engine weight. Here, "engine weight" refers to the total engine weight, which includes the bare engine, nacelle, nozzle, pylon, fuel systems, and miscellaneous equipment.

Table 4.9: Sensitivities [%/%] of environmental performance metric to engine weight.

Engine	$\dot{m}_{f.\text{CRZ}}$	Fleet Fuelburn	Climate Cost	Fleet NO$_x$	Air Quality Cost	Total Env. Cost
"A"	+0.139	+0.109	+0.0661	+0.207	+0.195	+0.124
"B"	+0.134	+0.132	+0.0707	+0.326	+0.298	+0.170
"C"	+0.236	+0.210	+0.155	+0.377	+0.369	+0.286

*Cruise fuel flow ($\dot{m}_{f.\text{CRZ}}$) presented is for mid-cruise case

Results show that an additional percentage weight leads to a higher fuel penalty for engine "C". This is because long-haul aircraft, compared to short-haul aircraft, are more susceptible to weight penalties due to higher fuel weight fractions and the fact that carrying extra fuel itself adds weight to the aircraft, creating a cycle where the aircraft needs even more fuel to compensate for the increased weight. It is important to distinguish between changes in engine weight measured in kilograms and percentages. When evaluating sensitivity per kilogram of engine weight change, engine "C" exhibits the lowest sensitivity. For engine "B", NO$_x$ and air quality cost sensitivities are similar to engine "C" despite a lower fuel burn sensitivity, due to the high T_3-EI(NO$_x$) sensitivity. This leads to total environmental cost sensitivity being the highest in engine "C", followed by "B" and "A".
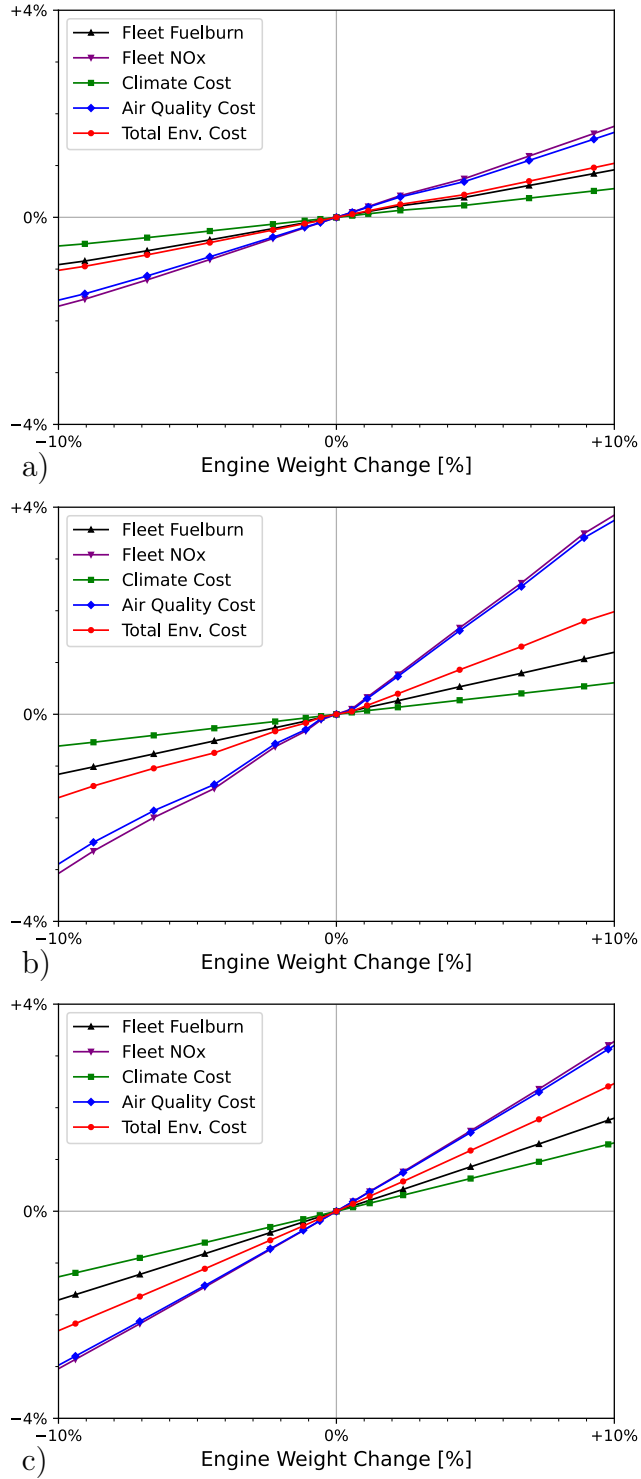
Figure 4-11: Performance metric change for change in fractional total engine weight change, for engine "A" (a), "B" (b), "C" (c).

Chapter 5

Sensitivity to External-to-Aviation Factors

5.1   Choice of Social Discount Rate

The discount rate is a societal preference set to reflect how a society values today's cost or benefit relative to that of the future, commonly considered as an implicit time horizon. The Net Present Value (NPV) approach, which employs the discount rate concept, calculates and sums up the year-by-year future damage assessments in present value terms. The discount rate plays a critical role in determining the resulting environmental costs as environmental damage occurs over extended time periods, with each damage pathway having its own impact timescales. For example, climate damage depends on the lifetime of each emission species, which extends to more than 800 years for CO_2, while human health implications due to air quality degradation occur over a much shorter timeframe. Accordingly, the choice of discount rate has a substantial impact on valuations of climate impact, while valuations of air quality impact are relatively less sensitive to it.

In Table 5.1, we examine the influence of using different discount rates on the NPV of climate and air quality damage. We also explore the impact of the discount rate on the relative balance between climate and air quality costs, which is best illustrated in the case of sensitivity to OPR. First, we observe that a higher discount rate

corresponds to a lower climate cost, as future climate damages are heavily discounted. Secondly, we find that the air quality cost remains relatively unchanged across different discount rates, as the air quality impact timescale is relatively short. Third, we observe a significant shift in the balance between climate and air quality costs, which is supported by the OPR sensitivity results presented in Table 5.1. This is because different discount rates lead to different weightings of climate and air quality costs, affecting the trade-offs between these two factors.

Table 5.1: Climate, air quality and total environmental cost for engine "A", for different discount rates.

DR	$\frac{\text{NPV}_{\text{Climate}}}{\text{RTK}}$ $\left[\frac{\$}{\text{(Tonne·km)}}\right]$	$\frac{\text{NPV}_{\text{Air Quality}}}{\text{RTK}}$ $\left[\frac{\$}{\text{(Tonne·km)}}\right]$	$\frac{\text{NPV}_{\text{Total}}}{\text{RTK}}$ $\left[\frac{\$}{\text{(Tonne·km)}}\right]$	$\text{NPV}_{\text{Total}}$ sensitivity to OPR
1%	1.35	0.176	1.53	+0.0749 [%/%]
2%	0.369	0.170	0.539	+0.245 [%/%]
3%	0.196	0.167	0.361	+0.358 [%/%]
5%	0.108	0.156	0.264	+0.476 [%/%]

The above analysis of using different discount rates for environmental impact assessment shows that higher discount rates will place more emphasis on air quality, while lower discount rates will prioritize long-term climate damage (i.e., from CO_2 emission). Stakeholders may adopt different discount rates based on their individual preferences, which will influence their decision-making. For example, decision-making or policy choice employing higher discount rates (i.e., short time horizon) increases the importance of air quality implications (i.e., NO_x) and short-lived climate forcers like contrails, hence pushing for the development of NO_x reduction technologies or contrail avoidance. Conversely, decision-making or policy choice employing lower discount rates (i.e., longer time horizon) will prioritize CO_2 (i.e., fuel burn) reduction, as the perceived impact of short-lived forcers and air quality impacts are reduced.

This is well demonstrated in Table 5.1, with the total environmental sensitivity to OPR increasing with higher discount rates. Nevertheless, results indicate that the sensitivity to OPR is consistently positive for all discount rates, suggesting that the statement "higher OPR leads to higher environmental damage" is valid across all shown discount rates, assuming the architecture and technology level of engine "A". These findings underscore the significance of selecting an appropriate discount rate in environmental impact assessment.

5.2   Background RCP & SSP Scenarios

Here, we analyze the influence of background RCP and SSP scenarios, associated with emissions and socio-economic scenarios, respectively. Environmental assessment is conducted assuming a tandem of SSP-RCP (for example, SSP1-RCP2.6, SSP2-RCP4.5, SSP5-RCP8.5 [72]). Figure 5-1 shows the future projections of RCP and SSP scenarios. Note that for the analyses below, engine "A" is again used as the representative case, with the emission year assumed to be 2050 (with fleet operation fixed to 2019) in order to better observe the divergence of the environmental cost result based on the selected RCP-SSP scenario.
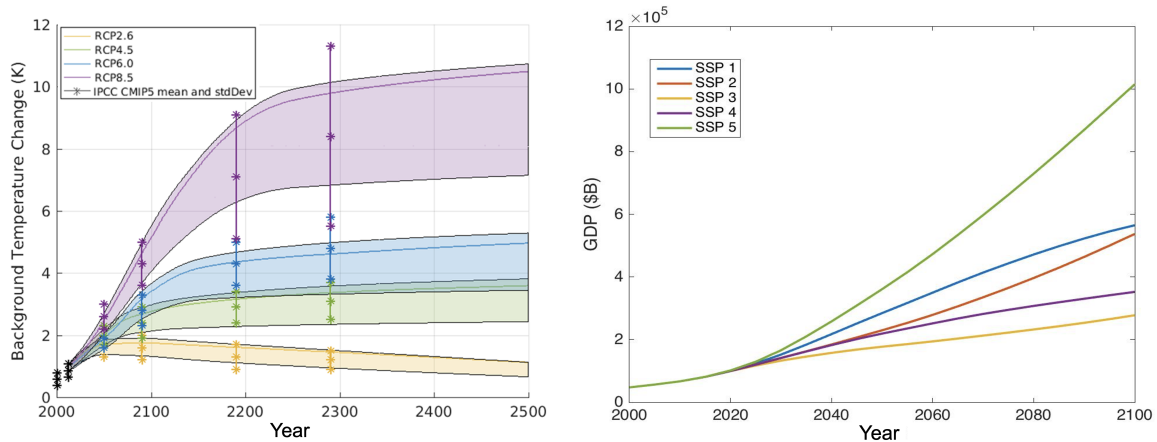
Figure 5-1: RCP scenarios from 2000-2500 (left), SSP scenarios from 2000-2100 (right)

5.2.1   RCP - GHG Concentration/Emissions Scenario

Table 5.2 presents the environmental impact based on different RCP scenarios, assuming an emission year of 2050. The climate damage increases from RCP2.6 to RCP8.5 (i.e., higher greenhouse gas concentration as shown in Figure 5-1) due to a combination of three factors: (1) Radiative Forcing (RF) due to an extra unit of CO_2, or marginal CO_2 impact, decreases with higher background concentration; (2) higher background concentration, however, leads to an increased background temperature change (ΔT), and due to the assumed quadratic relationship between temperature change and damage in the climate damage functions, higher climate damage follows; (3) higher background concentration results in longer lasting aviation CO_2.

Table 5.2: Climate, air quality and total environmental cost for engine "A", for different RCP scenarios.

Scenario	$\frac{NPV_{Climate}}{RTK}$ $\left[\frac{\$}{(Tonne \cdot km)}\right]$	$\frac{NPV_{Air\ Quality}}{RTK}$ $\left[\frac{\$}{(Tonne \cdot km)}\right]$	$\frac{NPV_{Total}}{RTK}$ $\left[\frac{\$}{(Tonne \cdot km)}\right]$	NPV_{Total} sensitivity to OPR
SSP2-RCP2.6	0.373	0.510	0.883	+0.436 [%/%]
SSP2-RCP4.5	0.460	0.510	0.970	+0.425 [%/%]
SSP2-RCP8.5	0.488	0.510	0.997	+0.401 [%/%]

*Emission year 2050 is assumed to better observe the effect of diverging background uncertainties. DR = 3%

On net, using an RCP scenario with higher background greenhouse gas concentration leads to increased marginal climate impacts, as shown in Table 5.2. On the other hand, air quality cost remains fixed over different RCP scenarios because of the fixed air quality adjoint sensitivity.

5.2.2 SSP - Background Socio-Economic Scenario

Table 5.3 shows the environmental impact using different Shared Socioeconomic Pathways (SSP), again assuming the emission year of 2050. SSP scenarios project future GDP and global population. Thus, selecting a scenario with a higher GDP forecast (SSP5, followed by SSP1 and SSP2) leads to an increase in both climate and air quality costs. This is because climate damage is calculated as a percentage of global GDP, and air quality damage is assessed using VSL which scales with GDP. For air quality cost, we should also mention that using a scenario with a higher population projection results in higher air quality cost as the affected population increases.

Table 5.3: Climate, air quality and total environmental cost for engine "A", for different SSP scenarios.

Scenario	$\frac{NPV_{Climate}}{RTK}$ $\left[\frac{\$}{(Tonne \cdot km)}\right]$	$\frac{NPV_{Air\ Quality}}{RTK}$ $\left[\frac{\$}{(Tonne \cdot km)}\right]$	$\frac{NPV_{Total}}{RTK}$ $\left[\frac{\$}{(Tonne \cdot km)}\right]$	NPV_{Total} sensitivity to OPR
SSP1-RCP4.5	0.528	0.648	1.18	+0.446 [%/%]
SSP2-RCP4.5	0.460	0.510	0.970	+0.425 [%/%]
SSP5-RCP4.5	0.799	0.808	1.61	+0.404 [%/%]

*Emission year 2050 is assumed to better observe the effect of diverging background uncertainties. DR = 3%

Chapter 6

Sustainable Aviation Fuels

Sustainable aviation fuels (SAFs) are considered as a means to reduce the environmental impact of commercial aviation in the near-to-mid term. These fuels have lower life-cycle emissions compared to fossil jet fuel and can be used in existing aircraft as drop-in fuels. When comparing the cost of SAF with Jet-A fuel, a comprehensive assessment is needed that considers their environmental impact and economic costs. Although we acknowledge that there are other components such as noise impacts (which can be assumed constant as only the fuel is changed) or social implications that we do not capture, we believe that for the purpose of this section, it is sufficient to define total social cost as the sum of the environmental (i.e., climate and air quality) cost and the marginal cost of fuel production. We estimate the SAF emissions by adjusting the Jet-A emissions per Table 2.3. Lifecycle emissions (LCA) and production costs of SAF as shown in Table 2.1 are used.

Figure 6-1 presents cost (NPV) of different social cost components per Revenue Tonne Kilometer (RTK), comparing between Jet-A and four alternative jet fuel pathways: Vegetable oil crops HEFA, Lignocellulosic FT, Sugarcane AF, and PtL. Three different social discount rates are used, namely 1%, 3%, and 5%. All analyses are conducted under the SSP2-RCP4.5 scenario [72], consistent with other results presented in this study. We analyze scenarios for both 2019 and 2050, where we adjust the emission year and fuel data accordingly but leave the flight operational scenario constant to 2019.
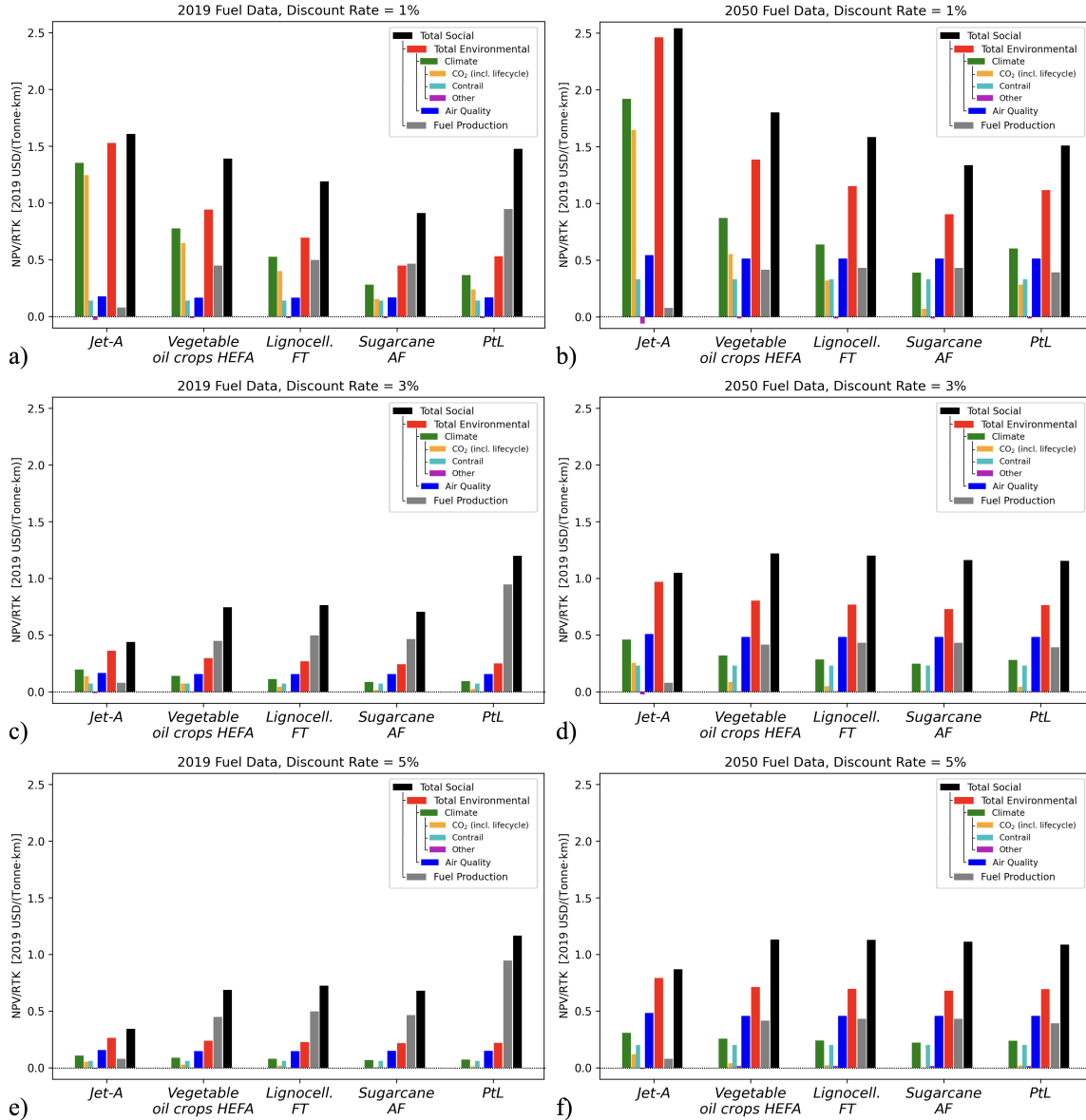
Figure 6-1: Comparison of total social cost of Jet-A and SAFs, a) 2019 fuel data, DR = 1%, b) 2050 fuel forecast, DR = 1%, c) 2019 fuel data, DR = 3%, d) 2050 fuel forecast, DR = 3%, e) 2019 fuel data, DR = 5%, f) 2050 fuel forecast, DR = 5%.

Figure 6-1(c) illustrates the scenario aligned with the default scenario of this study, for emission year 2019 using a 3% discount rate. We can first observe a low climate cost of SAFs primarily due to their reduced lifecycle CO_2 emissions compared to fossil Jet-A, resulting in a lower total environmental cost. Contrail climate impacts are assumed unchanged, the assumed absence of sulfur content leads to approximately 4% lower air quality costs and 6% higher climate costs, and lower soot EI leads to 1.4% lower climate cost, compared to fossil Jet-A. However, SAFs are much more

78

expensive to produce as shown in the marginal fuel production cost. Consequently, when factoring in the total environmental and production costs, all SAFs result in a higher total social cost compared to Jet-A for this case.

To observe the effect of discount rates, we compare Figures 6-1(a) and 6-1(e) with Figure 6-1(c). As mentioned before, lower discount rate values the future damage more, hence causing the long-term climate damage (i.e., CO_2) to be valued relatively high. Therefore, in terms of the climate and subsequent total environmental cost, the benefit of SAFs' reduced lifecycle CO_2 emissions is reflected most when a low discount rate is selected. In Figure 6-1(a), where we use a lower discount rate of 1%, SAFs' climate costs are lower by $40 - 80\%$ compared to Jet-A, resulting in lower total social cost of SAFs. Conversely, when we use a higher discount rate of 5% (Figure 6-1(e)), the reductions in climate costs are minimal as the emissions of short-term climate forcers are unchanged. With a lower perceived benefit of CO_2 lifecycle emissions reduction and relatively higher perceived costs of marginal costs of fuel production (incurring in the present), this results in higher total social costs of SAFs.

Comparing Figure 6-1(d) with Figure 6-1(c), projected reduction in lifecycle emissions and production costs for SAFs in year 2050 brings the total social cost of SAFs to be approximately on par with Jet-A under the discount rate of 3%. We can also observe that the environmental costs (both climate and air quality) are quantified to be higher than Figure 6-1(c) (year 2019, 3% discount rate), primarily from GDP and population growth.

In conclusion, using this approach, we can see that SAFs' lower life-cycle emissions leads to lower climate costs compared to fossil jet fuel. However, SAFs have higher marginal cost of production, leading to a higher total social cost when compared to fossil Jet-A in some cases, especially when near-term scenarios are analyzed. We can also see that the choice of discount rate is an important factor for this assessment, as it determines the relative value of future climate damage reduction with respect to other costs that occur in near-term (air quality impacts and fuel production). This analysis highlights the need for comprehensive assessments that consider both the environmental and production costs when comparing different fuels.

Chapter 7

Conclusions

In this thesis, we examined how different engine design parameters affect the environmental impact of aircraft. First, we analyzed the environmental performance of three different baseline engine-aircraft combinations, which represent a wide range of current-day aviation. Using an integrated environmental metric that normalizes the combined climate and air quality impact relative to aviation's productivity (i.e., RTK), we assessed the environmental performance of the baseline engines.

Then, we conducted a sensitivity analysis for each of the three engines, evaluating various design parameters. These parameters included primary cycle design factors such as OPR, FPR, and TET, secondary cycle parameters like material temperature capability and X_{cool}, and component polytropic efficiencies (η_p) and engine weight. For each design parameter change, we analyzed the resulting variations in fleet fuel consumption, NO_x emissions, as well as the associated climate and air quality costs. This analysis allowed us to ultimately assess the total environmental cost.

The underlying physical and modeling aspects responsible for the observed trends were explained, and the variation in trends across different engines were identified and analyzed in detail. The resulting tradeoff outcomes are shown to be dependent on the metrics of interest and the assumptions made when modifying a design parameter. Our findings indicate that the environmental sensitivities of each engine design parameter depends on the baseline engine design, including factors such as the engine's thermodynamic cycle, technology level, cooling flow, and aircraft/fleet

operations. Overall, climate damage was primarily driven by CO_2 emissions, with its relative change being less than the fuel burn/CO_2 sensitivities due to a fixed contrail impact. Air quality cost was predominantly influenced by NO_x emissions.

We find that for the OPR tradeoff, minimizing fuel burn does not necessarily lead to a reduction in total environmental impacts. From an environmental standpoint, results suggest (1) exploration of engine design space taking total environmental impact into account (i.e., limit engine OPR), and (2) investment in technologies that enable air quality impact to be lowered without the expense of higher fuel burn by decoupling the OPR-NO_x relationship. This can be achieved through the use of low-NO_x combustors or post-combustion emission treatment methods [79]. Further reductions in FPR, particularly for the narrow-body fleet, have the potential to yield additional fuel efficiency gains and environmental cost reductions. With anticipated technological advancements expected to decrease the engine weight and drag penalty associated with larger fan sizes, coupled with the utilization of different engine architectures, there is the possibility of even lower optimal FPR. However, further increase in fan diameter can pose challenges on aircraft installations. For the TET tradeoff, we find that the baseline TET of all three engines are close to the optimal TET in terms of fuel burn and environmental costs. Also, cooled HPT efficiency drop from a change in cooling flow and full-fleet/full-flight anlayses played critical roles in analyzing the TET tradeoff. Increase in material temperature capability, reduction in relative cooling flow (X_{cool}), and reduction in engine weight continue to benefit all analyzed metrics. For the turbomachinery component polytropic efficiencies (η_p), we find that the sensitivities are roughly proportional to the work done or extracted by each components, with HPC η_p identified as the dominant factor as it changes the combustor operating temperature (i.e., EI(NO_x)) and has a high pressure ratio.

We show that although the trend or direction of total environmental cost sensitivity agrees with that of the fleet fuel burn (except OPR), the magnitude is different. This disparity can result in inaccurate determination of optimal points or assessments regarding the relative impact and direction of design decisions. Consequently, this disparity has the potential to introduce errors in tradeoff studies and influence

decision-making processes. Our findings suggest that in order to accurately capture the actual environmental implications of an engine design, it is necessary to consider full-flight emissions rather than relying on single-point evaluations such as cruise, ADP, or sea-level-static. Even the SFC or fuel flow sensitivity of mid-cruise, which is often considered as a representative flight condition, is quite different from the actual fleet fuel burn sensitivity. For example, material temperature capability and X_{cool} tradeoff showed a $20-40\%$ difference between mid-cruise fuel flow and fleet fuel burn sensitivities, and the TET tradeoff showed different signs of sensitivity for engines "A" and "B". The discrepancy between mid-cruise NO_x emission sensitivity and fleet NO_x sensitivity was shown to be more significant than that of the fuel consumption, as $EI(NO_x)$ depends significantly on the engine/combustor operating condition (i.e., power settings and flight phase).

In addition to full-flight analysis, we also note the importance of full-fleet analysis when evaluating the environmental impacts. A fleet operations scenario based on flight schedule data or a realistic projection should be used, along with a good approximation of weight load factor. For instance, the fuel-optimum FPR varies depending on mission ranges, highlighting the significance of considering full-fleet analysis. We have also identified the average $N1/N1_{\text{ADP}}$, which is influenced by fleet operations, to be the underlying reason for the higher sensitivity of NO_x compared to fuel burn in the case of TET, material temperature capability, and X_{cool} tradeoffs. Therefore, relying on a single flight mission, such as a design range mission, would not fully capture certain tradeoffs. Furthermore, for air quality impact assessments, a global fleet scenario is necessary as the impact depends on the regional distributions of flights.

Additionally, designing and optimizing engines using missions that closely align with typical fleet operations is important. For example, when considering the FPR tradeoff, we observed that the optimal FPR varies depending on the mission range. Narrow-body fleets primarily operate on missions shorter than 500 nautical miles, even though the aircraft's design range is typically 3000 nautical miles. Therefore, it is important to carefully consider the missions that the engine is optimized to in order to ensure that the engine's actual environmental impact performance aligns with its

intended goals. However, we acknowledge the need for a balance between optimizing for fleet operations and accommodating the need for versatility in order to meet the demands of flexible fleet operations.

While simplicity is desired for emissions or environment relevant metrics or regulations, it is essential to determine whether they are adequate for capturing the actual environmental impacts. Given that the majority of aviation-related air quality and climate impacts come from cruise operations [46, 74], we find that existing LTO metrics, such as D_p/F_{oo}, do not accurately represent the full-fleet/full-flight performance and sensitivities. To bridge the gap between the full-fleet/full-flight analyses conducted in this study and the metrics or regulations, one possible approach could be to add a cruise-representative emissions data point (such as mid-cruise) to be reported and analyzed while utilizing the existing LTO data points. A full-fleet/full-flight representative metric can then be derived by introducing a weighting factor that takes fleet operations into account. For example, as we have seen in TET tradeoff, a narrow-body short-haul fleet may have a relatively higher weighting factor towards LTO, whereas a wide-body long-haul fleet may have a relatively higher weighting factor for cruise. This metric can be used for both the performance assessments of the baseline engines, and sensitivity studies, reducing the complexity of evaluating full-fleet/full-flight scenarios.

Our investigation shows that the choice of valuation, such as the discount rate, significantly influences the results. Although we report the resulting environmental cost using a 3% discount rate, it is important to acknowledge that there is no universally applicable discount rate for environmental impact evaluation. This is because quantifying environmental damage inherently depends on the valuation choice or societal time preference (i.e., discount rate), as aviation emissions result in damage pathways with various impact timeframes. Impacts of background emissions (RCP) and socio-economic (SSP) scenarios on total environmental cost sensitivities are found to be relatively small ($< \pm 10\%$). However larger changes were observed in absolute monetary damages.

The obtained sensitivities of aircraft environmental impacts to engine design pa-

rameters allow for an engine to be designed for minimum environmental cost. However, the sensitivities are not equivalent in scale. For instance, while the total environmental sensitivity of engine "B" to OPR and material temperature capability is almost the same in magnitude (approximately 1 [%/%]), it is not accurate to conclude that reducing OPR and improving material capability are equally effective measures to reduce environmental cost. The implications of a percentage change in each parameter are significantly different. Therefore, to obtain a complete picture, the derived sensitivities should be multiplied by a weighting factor, which accounts for how difficult or costly a percentage change in a given parameter is. For engine design parameter i, this can be expressed as:

$$\boldsymbol{S}\{(\text{Env. Impact}), (\text{Required Effort})_i\} =$$
$$\boldsymbol{S}(\text{Eng. Param}_i, \text{Required Effort}_i) \times \boldsymbol{S}(\text{Env. Impact}, \text{Eng. Param}_i)$$

where $\boldsymbol{S}(\text{Eng. Param}_i, \text{Required Effort}_i)$ refers to the required weighting factor and $\boldsymbol{S}(\text{Env. Impact}, \text{Eng. Param}_i)$ represents the sensitivity of the environmental impact to engine parameter i as obtained in this study. what we obtained in this study. This approach offers several benefits to stakeholders, including the ability to evaluate investment decisions and perform design tradeoffs to identify the best pathway for reducing environmental impact of aviation. By comparing the resulting $\boldsymbol{S}(\text{Env. Impact}, \text{Required Effort}_i)$ for different engine design parameters, stakeholders can determine which ones are most effective in reducing environmental impact, focusing efforts on those areas. By prioritizing the most impactful parameters and optimizing efforts, stakeholders can achieve the greatest reduction in environmental impact for a given input of resources.

The approach taken in this study allows for a sensitivity analysis of the design and operation of different aviation subsystems, focusing on the resultant environmental impact of aviation. Adopting the methodology used in this study, stakeholders can systematically incorporate environmental impact consideration from an early design stage, rather than restricting consideration to compliance with regulatory require-

ments through post-design analyses. By quantifying the environmental impact and its sensitivity to design parameters in terms of monetized cost-benefit, stakeholders can evaluate design-decisions using a common monetary basis that combines additional cost-benefit factors such as direct operating costs, investment or development costs, noise impacts, and maintenance costs. This enables the inclusion of estimated environmental impact as one of the target objective functions of aircraft engine design which can be expanded and applied to any other aviation subsystems' design and operation.

Future research can expand on the current study by including different engine configurations such as the geared turbofan or variable area nozzles. Although the current study assumes that an engine is installed on a single aircraft, analyzing various airframes that utilize the same engine could enhance the comprehensiveness of the findings. This could be done within an aircraft family (i.e., FADEC de-rated) or common cores across different aircraft types (i.e., LEAP engines on B737 MAXs, A320 NEOs, and A220s). Additionally, an extension to aircraft-level design parameters, including the choice of cruise altitude or cruise Mach number, can also be researched. Moreover, optimization of aircraft and engine design for minimum environmental cost can be explored. Although the estimated impact of contrails is included in the total environmental cost through climate cost, incorporating its sensitivity to engine design parameters will provide a more comprehensive understanding of the environmental impact of the engine. Furthermore, for FPR tradeoffs, including the noise impact sensitivity or investigating the significance of engine weight and drag models could also be potential areas of research.

References

[1] US EPA 2014. Guidelines for preparing economic analysis. https://www.epa.gov/environmental-economics/guidelines-preparing-economic-analyses, 2010, revised 2016. (accessed April 27 2023).

[2] US EPA 2016. Recommended income elasticity and income growth estimates: Technical memorandum online:. https://cfpub.epa.gov/si/si_public_file_download.cfm?p_download_id=532806, 2016. (accessed April 27, 2023).

[3] Ahrens, D., Mery, Y., Guénard, A., & Miake-Lye, R. C. A new approach to estimate particulate matter emissions from ground certification data: The nvPM mission emissions estimation methodology (MEEM). *Journal of Engineering for Gas Turbines and Power*, 145(3):031019, 2023.

[4] Alexander, B., Park, R.J., Jacob, D.J., Li, Q.B., Yantosca, R.M., Savarino, J., Lee, C.C.W., & Thiemens, M.H. Sulfate formation in sea-salt aerosols: Constraints from oxygen isotopes. *Journal of Geophysical Research: Atmospheres*, 110(D10), 2005.

[5] An ICF Report for ATAG Waypoint 2050. Fueling net zero: How the aviation industry can deploy sufficient sustainable aviation fuel to meet climate ambitions. https://aviationbenefits.org/media/167495/fueling-net-zero_september-2021.pdf, 2021. (accessed Jul 3 2022).

[6] Antoine, N. E., & Kroo, I. M. Aircraft optimization for minimal environmental impact. *Journal of aircraft*, 41(4):790–797, 2004.

[7] B737.org. Boeing 737 detailed technical data. http://www.b737.org.uk/techspecsdetailed.htm, 2022. (accessed April 26 2023).

[8] World Bank. GDP per capita, PPP (constant 2017 international $). https://data.worldbank.org/indicator/NY.GDP.PCAP.PP.KD, last updated June 30 2022. (accessed July 12 2022).

[9] Barrett, S. R., Yim, S. H., Gilmore, C. K., Murray, L. T., Kuhn, S. R., Tai, A. P., ... & Waitz, I. A. Public health, climate, and economic impacts of desulfurizing jet fuel. *Environmental science & technology*, 46(8):4275–4282, 2012.

[10] Baughcum, S. L., Tritz, T. G., Henderson, S. C., & Pickett, D. C. Scheduled civil aircraft emission inventories for 1992: Database development and analysis. *NASA No. NAS 1.26: 4700*, 1996.

[11] Bock, L. & Burkhardt, U. Reassessing properties and radiative forcing of contrail cirrus using a climate model. *Journal of Aircraft*, 121(16):9717–9736, 2016.

[12] Boeing Commercial Airplanes. 737 airplane characteristics for airport planning. 2021.

[13] Boeing Commercial Airplanes. 777-200LR / -300ER / -Freighter airplane characteristics for airport planning. 2022.

[14] Brasseur, G. P., Gupta, M., Anderson, B. E., Balasubramanian, S., Barrett, S., Duda, D., ... & Zhou, C. Impact of aviation on climate: FAA's aviation climate change research initiative (ACCRI) phase II. *Bulletin of the American Meteorological Society*, 97(4):561–583, 2016.

[15] Burkhardt, U. & Kärcher, B. Global radiative forcing from contrail cirrus. *Journal of Aircraft*, 1(1):54–58, 2011.

[16] Caiazzo, F., Agarwal, A., Speth, R. L., & Barrett, S. R. Impact of biofuels on contrail warming. *Environmental Research Letters*, 12(11):114013, 2017.

[17] CFM. Flight ops support document. https://www.smartcockpit.com/docs/ CFM_Flight_Ops_Support_B737.pdf, 2005. (accessed Oct 23, 2022).

[18] Chen, C. C. & Gettelman, A. Simulated radiative forcing from contrails and contrail cirrus. *Journal of Aircraft*, 13(24):12525–12536, 2013.

[19] Crippa, M., Janssens-Maenhout, G., Dentener, F., Guizzardi, D., Sindelarova, K., Muntean, M., Van Dingenen, R., & Granier, C. Forty years of improvements in european air quality: regional policy-industry interactions with global impacts. *Atmospheric Chemistry and Physics*, 16(6):3825–3841, 2016.

[20] Cumpsty, N. Jet propulsion, 2nd edition: A simple guide to the aerodynamic and thermodynamic design and performance of jet engines. *Cambridge University Press*, 2003.

[21] Cumpsty, N., & Heyes, A. Jet propulsion, 3rd edition. *Cambridge University Press*, 2015.

[22] Dellink, R., Chateau, J., Lanzi, E., & Magné, B. Long-term economic growth projections in the shared socioeconomic pathways. *Global Environmental Change*, 42:200–214, 2017.

[23] Dewanji, D., Rao, G.A., & van Buijtenen, J.P. Feasibility study of some novel concepts for high-bypass ratio turbofan engines. *ASME Turbo Expo 2009. GT2009-59166*, 2009.

[24] Dinc, A. The effect of flight and design parameters of a turbofan engine on global warming potential. *In IOP Conference Series: Materials Science and Engineering*, 1051(1):012051, 2021.

[25] Donovan, P., & Cackette, T. The effects of ambient conditions on gas turbine emissions - generalized correction factors. *Journal of Engineering for Power*, 100:640–646, 1978.

[26] Dray, L., Schäfer, A. W., Grobler, C., Falter, C., Allroggen, F., Stettler, M. E., & Barrett, S. R. Cost and emissions pathways towards net-zero climate impacts in aviation. *Nature Climate Change*, 12(10):956–962, 2022.

[27] M. Drela. Simultaneous optimization of the airframe, powerplant, and operation of transport aircraft. *RAeS 2nd Aircraft Structural Design Conference*, 2010.

[28] M. Drela. TASOPT 2.00. tech. rep. *Massachusetts Institute of Technology*, https://web.mit.edu/drela/Public/web/tasopt/, 2010.

[29] DuBois, D., & Paynter, G. C. "fuel flow method2" for estimating aircraft emissions. *SAE Transactions*, pages 1–14, 2006.

[30] Díez, N. G., Rao, A. G., & van Buijtenen, J. Conceptual study of counter-rotating turbofan engines. *In Turbo Expo: Power for Land, Sea, and Air*, 43963:255–264, 2010.

[31] EASA. Type-certificate data sheet No. IM.E.002 for GE90 series engine. https://www.easa.europa.eu/en/document-library/type-certificates/ engine-cs-e/easaime002-general-electric-ge90-series-engines, 2013. (accessed April 23, 2023).

[32] EASA. Type-certificate data sheet No. E.004 for CFM56-7B series engine. https://www.easa.europa.eu/en/document-library/type-certificates/ engine-cs-e/easae004-cfm-international-sa-cfm56-7b-series, 2019. (accessed Oct 23, 2022).

[33] EASA. Type-certificate data sheet No. E.115 for LEAP-1B series engine. https://www.easa.europa.eu/en/document-library/type-certificates/ engine-cs-e/easae115-leap-1b-series-engines, 2022. (accessed April 23, 2023).

[34] European Aviation Safety Agency (EASA). ICAO aircraft engine emissions databank. https://www.easa.europa.eu/domains/environment/ icao-aircraft-engine-emissions-databank, 2021. (accessed June 20 2022).

[35] US EPA. Advisory council on clean air compliance analysis response to agency request on cessation lag Washington D.C. https://nepis.epa.gov/Exe/ ZyPDF.cgi/P100JMYX.PDF?Dockey=P100JMYX.PDF, 2004. (accessed June 22, 2022).

[36] Etminan, M., Myhre, G., Highwood, E. J., & Shine, K. P. Radiative forcing of carbon dioxide, methane, and nitrous oxide: A significant revision of the methane radiative forcing. *Geophysical Research Letters*, 43(24):12–614, 2016.

[37] Falter et al. Power-to-liquid fuels and cryogenic hydrogen as aviation fuels: a global assessment of energy requirements, economics, infrastructure, and environmental performance. *Under Review*, 2022.

[38] Federal Aviation Administration. Type certification data sheet e00088en revision 5, April 2019.

[39] Federal Aviation Administration. Type certification data sheet e00056en revision 10, August 2016.

[40] Federal Aviation Administration. Type certification data sheet e00049en revision 20, December 2016.

[41] Bjorn Fehrm. Turbofan engine challenges, part 5. https://leehamnews.com/2016/12/02/bjorns-corner-turbofan-engine-challenges-part-5/, 2016. (accessed Oct 22, 2022).

[42] Institute for Health Metrics and Evaluation. Global burden of disease (gbd) study, global health data exchange, 2019. http://ghdx.healthdata.org/gbd-results-tool, 2019. (accessed June 22, 2022).

[43] Gauntner, J. W. Algorithm for calculating turbine cooling flow and the resulting decrease in turbine efficiency. *NASA No. NASA-TM-81453*, 1980.

[44] Geleynse, S., Brandt, K., Garcia-Perez, M., Wolcott, M., & Zhang, X. The alcohol-to-jet conversion pathway for drop-in biofuels: Techno-economic evaluation. *ChemSusChem*, 11(21):3728–3741, 2018.

[45] Gliebe, P. R., & Janardan, B. A. Ultra-high bypass engine aeroacoustic study. *NASA (No. NASA/CR-2003-212525)*, 2003.

[46] Grobler, C., Wolfe, P. J., Dasadhikari, K., Dedoussi, I. C., Allroggen, F., Speth, R. L., Eastham, S. D., Agarwal, A., Staples, M. D., Sabnis, J.& Barrett, S. R. Marginal climate and air quality costs of aviation emissions. *Environmental Research Letters*, 14(11):114031, 2019.

[47] Official Airline Guide. OAG scheduled flight data. 2019.

[48] Guynn, M. D., Berton, J. J., Fisher, K. L., Haller, W. J., Tong, M., & Thurman, D. R. Engine concept study for an advanced single-aisle transport. *NASA (No. L-19712)*, 2009.

[49] Guynn, M. D., Berton, J. J., Fisher, K. L., Haller, W. J., Tong, M. T., & Thurman, D. R. Refined exploration of turbofan design options for an advanced single-aisle transport. *NASA (No. NF1676L-12004)*, 2011.

[50] Guynn, M. D., Berton, J. J., Tong, M. J., & Haller, W. J. Advanced single-aisle transport propulsion design options revisited. *In 2013 Aviation Technology, Integration, and Operations Conference*, page 4330, 2013.

[51] Hartsel, J. Prediction of effects of mass-transfer cooling on the blade-row efficiency of turbine airfoils. *In 10th Aerospace Sciences Meeting*, page 11, 1972.

[52] Henze, D. K., Hakami, A., & Seinfeld, J. H. Development of the adjoint of GEOS-Chem. *Atmospheric Chemistry and Physics*, 7(9):2413–2433, 2007.

[53] Hoek, G., Krishnan, R. M., Beelen, R., Peters, A., Ostro, B., Brunekreef, B., & Kaufman, J. D. Long-term air pollution exposure and cardio-respiratory mortality: a review. *Environmental Health*, 12(1):1–16, 2013.

[54] Horlock, J. H., & Torbidoni, L. Calculations of cooled turbine efficiency. *Journal of Engineering for Gas Turbines and Power*, 130(1), 2008.

[55] Howard, P. H., & Sterner, T. Few and not so far between: a meta-analysis of climate damage estimates. *Journal of Aircraft*, 68(1):197–225, 2017.

[56] Hänsel, M.C., Drupp, M.A., Johansson, D.J., Nesje, F., Azar, C., Freeman, M.C., Groom, B., & Sterner, T. Climate economics support for the UN climate targets. *Nature Climate Change*, 10(8):781–789, 2020.

[57] IATA. Jet fuel price monitor. https://www.iata.org/en/publications/economics/fuel-monitor/. (accessed Jul 3 2022).

[58] ICAO. Annex 16 to the convention on international civil aviation, volume ii - aircraft engine emissions fourth edition (montreal: International civil aviation organization) 978-92-9258-314-9. 2017.

[59] ICAO. CORSIA default life cycle emissions values for CORSIA eligible fuels. Retrieved from the International Civil Aviation Organization https://www.icao.int/environmental-protection/CORSIA/Documents/ICAO%20document%2006%20-%20Default%20Life%20Cycle%20Emissions%20-%20March%202021.pdf, 2021. (accessed Jul 3 2022).

[60] ICAO. Report on the feasibility of a long-term aspirational goal (LTAG) for international civil aviation CO_2 emission reductions. Retrieved from the International Civil Aviation Organization https://www.icao.int/environmental-protection/LTAG/Documents/REPORT%20ON%20THE%20FEASIBILITY%20OF%20A%20LONG-TERM%20ASPIRATIONAL%20GOAL_en.pdf, 2022. (accessed Jul 3 2022).

[61] International Civil Aviation Organization (ICAO). CORSIA eligible fuels—life cycle assessment methodology. *CORSIA Supporting Document*, 2019.

[62] International Air Transport Association (IATA). Industry statistics fact sheet. https://www.iata.org/en/iata-repository/publications/economic-reports/ airline-industry-economic-performance---october-2021---data-tables/, 2020.

[63] Jane's). Jane's aero-engines. 1996-97 (New Annual Subscription).

[64] Jenkinson, L. R., Simpkin, P., & Rhodes, D. Civil jet aircraft design (vol. 338). *London, UK: Arnold.*, 1999.

[65] Jones, S. M. An introduction to thermodynamic performance analysis of aircraft gas turbine engine cycles using the numerical propulsion system simulation code. *No. NASA/TM-2007-214690*, 2007.

[66] Kim, B.Y., Fleming, G.G., Lee, J.J., Waitz, I.A., Clarke, J.P., Balasubramanian, S., Malwitz, A., Klima, K., Locke, M., Holsclaw, C.A., & Maurice, L.Q.,. System for assessing aviation's global emissions (SAGE), version 1.5: technical manual. *System for assessing Aviation's Global Emissions (SAGE), version 1.5: technical manual (No. DOT-VNTSC-FAA-05-14), United States. Federal Aviation Administration.*, 2005.

[67] Koopmann, J., Zubrow, A., Hansen, A., Hwang, S., Ahearn, M., & Solman, G. Aviation environmental design tool (AEDT) 2b user guide. *(No. DOT-VNTSC-FAA-15-07)*, 2016.

[68] Lee, D. S., Fahey, D. W., Skowron, A., Allen, M. R., Burkhardt, U., Chen, Q., ... & Wilcox, L. J. The contribution of global aviation to anthropogenic climate forcing for 2000 to 2018. *Atmospheric Environment*, 244:117834, 2021.

[69] Mahashabde, A., Wolfe, P., Ashok, A., Dorbian, C., He, Q., Fan, A., Lukachko, S., Mozdzanowska, A., Wollersheim, C., Barrett, S.R., Locke, M., & Waitz, I. A. Assessing the environmental impacts of aircraft noise and emissions. *Progress in Aerospace Sciences*, 47(1):15–52, 2011.

[70] Marais, K., Lukachko, S. P., Jun, M., Mahashabde, A., & Waitz, I. A. Assessing the impact of aviation on climate. *Meteorologische Zeitschrift*, 17(2):157–172, 2008.

[71] Marchionna, N. R., Diehl, L. A., & Trout, A. M. Effect of inlet-air humidity, temperature, pressure, and reference mach number on the formation of oxides of nitrogen in a gas turbine combustor. *NASA Report No. E-7465*, 1973.

[72] Masson-Delmotte, V., Zhai, P., Pirani, A., Connors, S. L., Péan, C., Berger, S., ... & Zhou, B. Climate change 2021: The physical science basis. *Contribution of Working Group I to the Sixth Assessment Report of the Intergovernmental Panel on Climate Change, Cambridge University Press*, 2021.

[73] Mavris, D. N., DeLaurentis, D., Crossley, W. A., & Alonso, J. J. Project 010: Aircraft technology modeling and assessment: Phase i

report. https://s3.wp.wsu.edu/uploads/sites/192/2017/10/ASCENT_P10_ 2017_PhaseI_Final_Report.pdf, 2017. (accessed Oct 23, 2022).

[74] Miller, C. J., Prashanth, P., Allroggen, F., Grobler, C., Sabnis, J. S., Speth, R. L., & Barrett, S. R. An environmental cost basis for regulating aviation NOx emissions. *Environmental Research Communications*, 4(5):055002, 2022.

[75] Murray, L. T., Jacob, D. J., Logan, J. A., Hudman, R. C., & Koshak, W. J. Optimized regional and interannual variability of lightning in a global chemical transport model constrained by LIS/OTD satellite data. *Journal of Geophysical Research: Atmospheres*, 117:20307, 2012.

[76] Nordhaus, W. D. Revisiting the social cost of carbon. *Proceedings of the National Academy of Sciences*, 114(7), 2017.

[77] Pantalone, G., Blanco, E. D. L. R., & Wilcox, K. TASOPT engine model development: A PARTNER project 48 report (No. PARTNER-COE-2016-004). https://ascent.aero/documents/2020/02/tasopt-engine-model-development. pdf/, 2016. (accessed Oct 22, 2022).

[78] Prashanth, P., Eastham, S. D., Speth, R. L., & Barrett, S. R. Aerosol formation pathways from aviation emissions. *Environmental Research Communications*, 4(2):021002, 2022.

[79] Prashanth, P., Speth, R. L., Eastham, S. D., Sabnis J. S.,& Barrett, S. R. Post-combustion emissions control in aero-gas turbine engines. *Energy & Environmental Science 14, no. 2*, pages 916–930, 2021.

[80] Randerson, J. T., Van Der Werf, G. R., Giglio, L., Collatz, G. J., & Kasibhatla, P. S. Global fire emissions database, version 4.1 (GFEDv4). *ORNL DAAC*, 2015.

[81] Robinson, L. A., & Hammitt, J. K. The effect of income on the value of mortality and morbidity risk reductions. prepared for industrial economics, inc., Cambridge, MA: Washington, DC, on behalf of the US Environmental Protection Agency. https://yosemite.epa.gov/sab/SABPRODUCT.NSF/0/ 0CA9E925C9A702F285257F380050C842/\protect\T1\textdollarFile/IEc_ Income%20elasticity%20Report%20_final.pdf, 2015. (accessed July 12, 2022).

[82] Rusnak, J. P., & Shadowen, J. H. Development of an advanced annular combustor. *NASA Report No. NASA-CR-72453*, 1969.

[83] Schumann, U., Penner, J. E., Chen, Y., Zhou, C. & Graf, K. Dehydration effects from contrails in a coupled contrail-climate model. *Journal of Aircraft*, 15(9):11179–11199, 2015.

[84] Simone, N. W., Stettler, M. E., & Barrett, S. R. Rapid estimation of global civil aviation emissions with uncertainty quantification. *Transportation Research Part D: Transport and Environment*, 25:33–41, 2013.

[85] Stettler, M. E. J., Eastham, S., & Barrett, S. R. Air quality and public health impacts of UK airports. Part I: Emissions. *Atmospheric Environment*, 45(31):5415–5424, 2011.

[86] Stratton, R. W., Wolfe, P. J., & Hileman, J. I. Impact of aviation non-CO2 combustion effects on the environmental feasibility of alternative jet fuels. *Environmental Science & Technology*, 45(24):10736–10743, 2011.

[87] Thacker, R. P., & Blaesser, N. Modeling of a modern aircraft through calibration techniques. *In AIAA Aviation 2019 Forum*, page 2984, 2013.

[88] Thoma, E. M., Grönstedt, T., & Zhao, X. Quantifying the environmental design trades for a state-of-the-art turbofan engine. *Aerospace*, 7(10):148, 2020.

[89] Torenbeek, E. Synthesis of subsonic airplane design. *Martinus Nijhoff publishers*, 1975.

[90] Turner, M. C., Jerrett, M., Pope III, C. A., Krewski, D., Gapstur, S. M., Diver, W. R., Beckerman, B. S., Marshall, J. D., Su, J., Crouse, D. L., & Burnett, R. T. Long-term ozone exposure and mortality in a large prospective study. *American journal of respiratory and critical care medicine*, 193(10):1134–1142, 2016.

[91] U.S. Bureau of Economic Analysis. Real gross domestic product per capita [A939RX0Q048SBEA]. retrieved from FRED, Federal Reserve Bank of St. Louis; https://fred.stlouisfed.org/series/A939RX0Q048SBEA, 2022. (accessed July 12 2022).

[92] U.S. EPA 2009). Recommended best practice for quantifying speciated organic gas emissions from aircraft equipped with turbofan, turbojet and turboprop engines. version 1.0. *Federal Aviation Administration Office of Environment and Energy and U.S. Environmental Protection Agency Office of Transportation and Air Quality*, 2009.

[93] US EPA 2015. 2011 national emissions inventory, version 2 technical support document (North Carolina). https://www.epa.gov/sites/default/files/2015-10/documents/nei2011v2_tsd_14aug2015.pdf, August 2015. (accessed April 26 2023).

[94] US EPA 2017. Guidelines for preparing economic analyses: Mortality risk valuation estimates (appendix b). https://www.epa.gov/sites/default/files/2017-09/documents/ee-0568-22.pdf, 2017. (accessed July 12, 2022).

[95] Wadia, A. R. Technologies for the next engine generation. *In 29th Congr. Int. Counc. Aeronaut. Sci. ICAS.*, 2014.

[96] Watterson, J., Walker, C., & Eggleston, S. Revision to the method of estimating emissions from aircraft in the UK greenhouse gas inventory. *Report to Global Atmosphere Division, UK Defra. Report number ED47052*, 2004.

[97] Whellens, M. W., & Singh, R. Propulsion system optimisation for minimum global warming potential. *In Proceedings of ICAS 2002 Congress, Toronto*, 2002.

[98] Wilcock, R. C., Young, J. B., & Horlock, J. H. The effect of turbine blade cooling on the cycle efficiency of gas turbine power cycles. *Journal of Engineering for Gas Turbines and Power*, 127(1):109–120, 2005.

[99] Wilfert, G., Sieber, J., Rolt, A., Baker, N., Touyeras, A., & Colantuoni, S. New environmental friendly aero engine core concepts. *ISABE Paper, (2007-1120)*, 2007.

[100] Wilkerson, J. T., Jacobson, M. Z., Malwitz, A., Balasubramanian, S., Wayson, R., Fleming, G., Naiman, A. D., & Lele, S. K.,. Analysis of emission data from global commercial aviation: 2004 and 2006. *Atmospheric Chemistry and Physics*, 10(13):6391–6408, 2010.

[101] Wolfe, P. J. Aviation environmental policy effects on national-and regional-scale air quality, noise, and climate impacts. *Master's Thesis, Massachusetts Institute of Technology*, 2012.

[102] Wolfe, P. J. Aviation environmental policy and issues of timescale. *Doctoral dissertation, Massachusetts Institute of Technology*, 2015.

[103] York, M. A., Hoburg, W. W., & Drela, M. Turbofan engine sizing and tradeoff analysis via signomial programming. *Journal of Aircraft*, 55(3):988–1003, 2018.

[104] Zender, C. S., Bian, H., & Newman, D. Mineral dust entrainment and deposition (DEAD) model: Description and 1990s dust climatology. *Journal of Geophysical Research: Atmospheres*, 108(D14), 2003.

Appendix A

P3T3 NO$_x$ correlation

For Engine "A": $\mathrm{EI(NO}_x) = P_3^{0.4} \times \exp\left[19(h_{\mathrm{SL}} - h_{\mathrm{Alt}})\right] \times [(5.2741e - 08) \times T_3^3 - (9.8573e - 05) \times T_3^2 + (6.1924e - 02) \times T_3 - (1.2512e + 01)]$

For Engine "B":

- N1 $\leq$ 60[%] (low-power mode, pilot-only):

  - $\mathrm{EI(NO}_x) = P_3^{0.4} \times \exp\left[19(h_{\mathrm{SL}} - h_{\mathrm{Alt}})\right] \times [(1.3706e - 05) \times T_3^2 - (1.4604e - 02) \times T_3 + (4.2111e + 00))]$

- N1 $>$ 60[%] (high-power mode, pilot + main),

  - T$_3$ < 824.6 [K] (Extrapolation required):

    · Low NO$_x$ bound: $\mathrm{EI(NO}_x) = P_3^{0.4} \times \exp\left[19(h_{\mathrm{SL}} - h_{\mathrm{Alt}})\right] \times [(7.4940e - 08) \times \exp[1.9355e - 02 \times T_3]]$

    · Mid NO$_x$: Averaged between low and high NO$_x$ bounds

    · High NO$_x$ bound: $\mathrm{EI(NO}_x) = P_3^{0.4} \times \exp\left[19(h_{\mathrm{SL}} - h_{\mathrm{Alt}})\right] \times [(5.5656e - 05) \times T_3 + (2.4638e - 01))]$

  - T$_3$ > 824.6 [K]:

    · $\mathrm{EI(NO}_x) = P_3^{0.4} \times \exp\left[19(h_{\mathrm{SL}} - h_{\mathrm{Alt}})\right] \times [(5.5891e - 05) \times T_3 + (2.5528e - 01))] \times \exp\left[19(h_{SL} - h_{Alt})\right.$

For Engine "C": $\mathrm{EI(NO}_x) = P_3^{0.4} \times \exp\left[19(h_{\mathrm{SL}} - h_{\mathrm{Alt}})\right] \times [(1.1084e - 07) \times T_3^3 - (2.1272e - 04) \times T_3^2 + (1.5062e - 01) \times T_3 - (3.3474e + 01))]$